IN-OCEAN EXPERIMENTS OF A WAVE ENERGY CONVERSION DEVICE WITH A DROGUE AND WAVE POWER CALCULATIONS

A THESIS SUBMITTED TO THE GRADUATE DIVISON OF THE UNIVERSITY OF HAWAIʻI AT MĀNOA IN PARTIAL FULFILLMENT OF THE REQUIREMENTS FOR THE DEGREE OF

MASTER OF SCIENCE

IN

OCEAN AND RESOURCES ENGINEERING

AUGUST 2013

By

Jerica Nolte

Thesis Committee:

R. C. Ertekin, Chairperson
G. C. Nihous
H. R. Riggs

ACKNOWLEDGMENTS

I would like to thank my parents for allowing me to realize my own potential. All the support they have provided me over the years was the greatest gift anyone has ever given me.

I owe special thanks to my advisor Professor R.C. Ertekin, for his support, patience, and encouragement throughout my graduate studies. It is not often that one finds an advisor that always finds the time for listening to the little problems and roadblocks that unavoidably crop up in the course of performing research. His technical and editorial advice was essential to the completion of this thesis and has taught me innumerable lessons.

My thanks also go to the members of my committee, Professor Gerard C. Nihous and Professor H. Ronald Riggs for their insightful participation and support in this project and their review of my thesis.

I would like to thank Srinivasamurthy A. Chitrapu for kindly answering all of my questions and explaining to me parts of the programming needed for this project. Also, I would like to thank Andrew Schwartz for helping me by running multiple meshes through HYDRAN and working with me to get the results I needed.

This research was sponsored by the Office of Naval Research through TREX Enterprises of Maui through a grant to Professor R.C. Ertekin at the University of Hawaii. The program director at ONR was Dr. Ron Joslin. Thanks also go to Michael Engelmann and Ned Davis of Trex Enterprises of Maui for their kind assistance in the

experiments. The generous help of the UH scientific dive team members Kai Gemba and Narineh Nazarien during the experiments is very much appreciated.

ABSTRACT

This research describes the experimental and numerical modeling of a heaving point source wave energy conversion (WEC) device developed by Trex Enterprises of Maui and tested by the University of Hawaii at Manoa. The principle of operation of the WEC device is to convert the vertical heave displacement into a rotational action, which generates electrical power. The heave displacement is created by the WEC system riding incoming waves relative to an anchoring system. Two deployment cases of the single WEC device were ocean tested with the goal of collecting power data based on the type of the anchoring method. The anchoring methods are referred to as the single-body case (moored system) and double-body case (drogue anchored system). The experiments were carried out on the South shore of Oahu during the summer of 2012. The WEC system was equipped with sensors to measure and record the heave displacements of the WEC system, the generated power output, and the surface elevation. The real time experimental data were collected and analyzed to determine the power generation profile, the WEC system's heave displacements, surface elevation, and heave response amplitude operator (RAO) for both cases. A numerical modeling program was built to perform hydrodynamic analysis in the time domain in irregular seas for the single-body or double-body case. The program solves for the individual body motion. It is used to predict the WEC device's power production over the time series.

TABLE OF CONTENTS

LIST OF TABLES

LIST OF FIGURES

LIST OF ABBREVIATIONS AND SYMBOLS

α	Spring to Mooring force ratio	
β	Gearing Ratio	
Δt	Time interval	s
Δ	Weight of the water displaced	N
ϵ	Random phase	rad/s
η	Sea surface elevation	m
γ	Ratio of the spool to rotary sensor	
∞	Infinity	
ρ	Density	kg/m^3
ϕ	Velocity potential	
σ_i	Angular frequency of the spectrum	rad/s
σ_n	Peak frequency	rad/s
σ_f	maximum frequency where b become zero	rad/s
σ_{st}	standard deviation	
τ	time series of the Kernel function	s
τ_{max}	Maximum value of τ	s
θ	angle of the towing line	degrees
$\dot{\theta}$	Angular velocity of the spool	s^{-1}
$A(\sigma)$	Amplitude of the (σ) component of the spectrum	
C_{DD}	Generator viscous damping coefficient	Ns/m
C_θ	Angular momentum of spool	N-m-s
H_s	Significant wave height	m
T_p	Peak period	s
a	Frequency dependent added mass	kg
A_{33}	Genuine added mass	kg
A_p	Projected area	m
A_w	Water plane area	m
b	Frequency dependent damping	kg/s
C_D	Drag coeffienct	
D	Drogue inlet diameter	m
d	Drogue outlet diameter	m
$d\omega$	interval of ω	
DC	Direct current	
Drf	Drift	m
$DWEC_D$	Detrended WEC displacement	m
F	Force	N
f(x)	Function	
FBD	Free body diagrams	

$F_{constant}$	Force of the constant force spring	N
F_D	Diffraction force	N
F_{gen}	Vertical force of WEC generator	N
F_{hs}	Hydrostatic forces	N
F_o	Sum of forces that do not include acceleration terms	N
F_R	Hydrodynamic radiation forces	N
F_{VD}	Vertical viscous drag force	N
F_{WEC}	Force of the WEC PTO	N
F_{w_k}	Wave exciting forces	N
g	Acceleration due to gravity	m/s^2
GPS	Global positioning system	
$H(\dot{z}(t))$	Heavy side function of velocity	
H	Height of drogue	m
H^D	Diffraction force transfer function	N/m
H^{FK}	Froude-Krylov force transfer function	N/m
HI^D	Imaginary part of the diffraction force transfer function	N/m
HI^{FK}	Imaginary part of the Froude-Krylov force transfer function	N/m
HR^D	Real part of the diffraction force transfer function	N/m
HR^{FK}	Real part of the Froude-Krylov force transfer function	N/m
i	index of spectral component	
IRPM	instantaneous RPM	
k	wave number	
$K(\tau)$	Kernel function	
K_m	Spring coefficient of the mooring	
m	Body mass	kg
M	Memory function	
n	Unit normal vector	
N	Number of wave components	
n	Degrees rotated	degrees
NASA	National Aeronautics and Space Administration	
NIST	National Institute of Standards and Technology	
NOAA	National Oceanic and Atmospheric Administration	
ODE	Ordinary differential equation	
P	Power	W
PTO	Power take-off	
R	Radial distance from body center	m
R_L	Load resistor value	Ω
RAO	Response amplitude operator	m/m
Rev	Revolution per time step	
RMS	Root mean square	
RPM	Revolutions per minute	
r_{rs}	Radius of the rotary sensor	m
r_{spool}	Spool radius that connects to the spring line	m

r_{morr}	Spool radius that connects to the mooring line	m
$S(\sigma)$	Spectrum	m^2s
S_e	Spectrum of the surface elevation	m^2s
SVP	Surface Velocity Program	
SWL	Still water level	
S_z	Spectrum of the heave displacement	m^2s
t	Time	s
Tor	Torque	N-m
T	Tension	N
Td	Tide	m
V	Relative velocity	m/s
W	Weight	N
WEC	Wave Energy Converter	
WEC_D	WEC heave displacement	m
wv	Vertical water particle velocity	m/s
z	Vertical coordinate	m
$\ddot{z}(t)$	Body acceleration	m/s^2
$\dot{z}(t)$	Body velocity	m/s
z(t)	Body displacement	m
$\dot{z}_{rel}$	Relative velocity between Body A and Body B	m/s
Z_s	Double amplitude of heave displacement	m^2s

CHAPTER 1

INTRODUCTION

Over the years, many systems were developed to extract power from waves, tides, and currents of the oceans. McCormick (1981) states that wave energy has become a main focus due to higher energy densities and predictability. Wave energy is the transport of energy by ocean surface waves, and that energy can be captured for electricity generation. A device that is able to convert wave energy is typically called a wave energy converter (WEC). A modern scientific pursuit of wave energy was pioneered by Yoshio Masuda's experiments in the 1940s. Masuda tested multiple wave energy devices at sea, with several hundred units used to power navigation lights (Washio, 1998). One of the more famous WEC devices was Stephen Salter's 1974 Duck. In small scale lab tests, the Duck's curved cam-like body absorbed 90% of wave energy and converted it to electricity with 81% efficiency (Salter, 1978).

Government organizations in the U.S., such as the National Oceanic and Atmospheric Administration (NOAA), National Aeronautics and Space Administration (NASA), and the U.S. Navy, use buoys throughout the world to monitor environmental conditions and disaster events. The launching of a global array of 1250 drifting buoys was completed in September 2005 and some 300 new drifters are deployed annually (NASA, 2013). Modern Surface Velocity Program (SVP) drifters include a holey-sock drogue centered at 15 m depth and surface float with a 30 cm to 40 cm diameter. It could contain batteries in 4-5 packs, each with 7-9 alkaline D-cells,

a transmitter, a thermistor to measure sea surface temperature, and possibly other instruments measuring barometric pressure, wind speed and direction, salinity, and ocean color. Once deployed, a modern drifter lives an average of 400 days before ceasing transmission (NOAA, 2012). Acoustic sensors can draw up to 100-200 W of continuous power during operation, thus limiting the battery life in most cases 12 to 24 hours on one battery charge. Recharging is so impractical and costly that many acoustic buoys are designed to sink to the bottom after a short period of operation. The cost and environmental impact of sending batteries and electrical equipment to the bottom of the ocean is a strong motivation for developing a freely floating wave energy conversion buoy that would trickle-charge the batteries (Davis, Ertekin, and Riggs, 2009). A freely floating WEC buoy would use a drogue's drag properties to provide a stable anchor point relative to the wave motion. A monitoring station with a WEC device could sustain a longer design life, save on the maintenance costs, and have decreased environmental impact.

1.1 Background

In 2008, the Office of Naval Research awarded a grant to Trex Enterprises Corporation in association with the University of Hawaii to develop a wave energy conversion prototype capable of generating energy from wave induced heaving motion in shallow water environments. Furthermore, the project called for the creation of a numerical model to estimate the device motions and power output.

Phase 1 concluded in early 2009, resulting in a WEC that successfully produced 20-50 W of peak power during sea trials performed at Kilo Nalu Nearshore Observatory on Oahu, Hawaii. Developed in HYDRAN (2008), a linear potential theory numerical model was used to predict WEC motions (Symonds, Davis, and Ertekin, 2010).

Phase 2 of this project began in August 2009. Phase 2 aimed to improve the Phase 1 prototype and produce between 100-200 W of power. As in Phase 1, the project includes the creation of a numerical model to accurately predict the system motions and resulting power output. Trex has assumed the responsibility of developing and building the wave energy conversion prototype, while the University of Hawaii at Manoa has the responsibility of experimental testing and building the numerical model.

In August 2011, Phase 2 continued and Phase 3 began. The experiments completed in June 2012 concluded Phase 2. Phase 3 called for the WEC to produce 100-200 W of power and a comparison between different testing scenarios, a moored WEC and freely floating WEC. The different anchoring methods, referred to as the single-body case and double-body case, were tested during ocean trials to compare the results. Both methods had the same WEC setup, referred to in this paper as the WEC system. The WEC system consisted of a Polyform A5 buoy rigidly attached to the WEC frame which supported water-tight housings, ballast, power take-off (PTO) and measuring equipment. The single-body case consisted of the WEC system held in place via a taut mooring line and extracting energy as a wave passes. The double-body case consisted of the WEC system held by a sea anchor or drogue that allowed

the system to be partially free floating and still have the adequate vertical resistance necessary to extract energy as a wave passes. The numerical model for Phase 3 was built in Matlab and solves the equations of motion in the time domain to include the nonlinearities in the system. From the WEC heave motion, the power is predicted for the system.

1.2 Literature Review

A review of numerical methods is relevant to solve the equations of motion for a WEC buoy in the time domain. This problem has been studied extensively in the frequency domain; however, solving the problem in the time domain allows for the inclusion of nonlinearities and a more accurate comparison between the theoretical and experimental data. The main difference between these two methods is the procedure to solve for the wave exciting and hydrodynamic forces. Cummins (1962) proposed a method using the impulse response function and decomposition of a ship's velocity potential to represent the small, arbitrary motions of a ship. He derived the relations between the frequency dependent added mass and damping coefficients and time domain kernel functions. An application of this method can be seen in papers by Van Oortmerssen (1979), Chitrapu (1992), and Greeson (1997) among others. Ogilvie (1964) expanded Cummins' theory and found that the force at time t is given by a Kernel function representing the hydrodynamic coefficients and conditions at t=0. The Kernel functions (or retardation functions) are integrated from t=0 to present

and account for the "memory" effect of prior waves.

Otto de Kat (1988) and Chitrapu (1992) solved the equations of motion for six degrees of freedom in the time domain for a floating ship and platform, respectively. Using potential theory and strip theory, each derived the Froude-Krylov, radiation, and diffraction forces for regular and irregular seas to predict large-amplitude motions of a floating body. The derived time domain simulation algorithms solved the equations of motion and evaluated the memory effect integral to find the body motions, see e.g., Chitrapu and Ertekin (1995).

Van Oortmerssen (1979) and Greeson (1997) studied the relative motion of two adjacent bodies, floating in waves. If two bodies are floating in waves near each other, there will be extra fluid loading on the separate bodies caused by the presence of the neighboring structure. The equations of motion for each body reflect the loading exerted by the body's own radiated waves and the second body's radiated waves as well.

Vicente et al. (2010) and Keller (2011) researched taut moored buoys with a linear spring and damper power take-off devices. Keller (2011) numerically modeled a circular cylinder WEC buoy in regular waves in the frequency domain to find the time averaged power absorbed by the buoy. Vicente et al. (2010) numerically modeled a WEC system consisting of a hemispherical buoy in regular and irregular waves. They compared the frequency domain and time domain numerical results of buoy displacements and power absorption. Vicente et al. (2010) concluded that the nonlinearities greatly affect the horizontal oscillations, and the vertical oscillations greatly depend

on the wave frequency. Also, that the power produced is directly determined by the body motion.

Research on different types of buoy and drogue combinations was done to determine the forces on the submerged body subjected to the forces on surface (wave, swell, and current) and between the buoy and drogue. Vachon (1975), Vachon (1977), Holler (1985) experimentally determined that the vertical and horizontal drag coefficients for multiple drogues. The drag coefficients they found determined which drogue would be best suited for the known environmental conditions. The vertical drag coefficient for the conical drogue determines the maximum vertical drag force the drogue can produce. Montgomery and Stroup (1962) concluded that a drogue can be scaled to achieve stability where the drogue's motion does not deviate from the direction of the connecting line's tension.

1.3 Objectives

The objectives of this work are to confirm that the WEC system design can produce 100-200 W in small seas, can produce power whether moored or freely floating, and to build a numerical model that calculates body motions and power generation in any wave climate.

CHAPTER 2

EXPERIMENTS

In the single-body case, the WEC system was moored to an anchor on the sea floor. In the double-body case, the WEC system was moored to a conical drogue or sea anchor. Both cases are shown in Fig. 2.1. The drawings are not to scale.

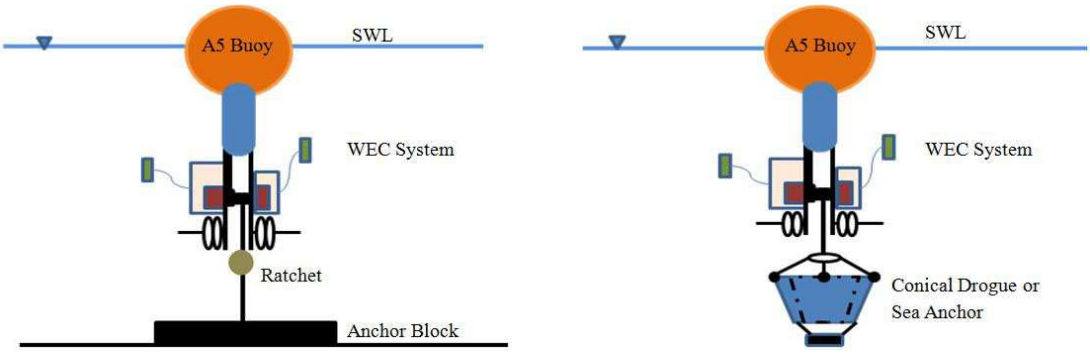

Figure 2.1. Model of single-body case (right) and double-body case (left)

The WEC system used during the June 2012 ocean trials is shown in Fig. 2.2. The WEC system consists of a Polyform A5 buoy (with a diameter of 68.6 cm and height of 91.4 cm), PVC mount, WEC frame, ballast, and WEC device that are all rigidly connected together to form one body.

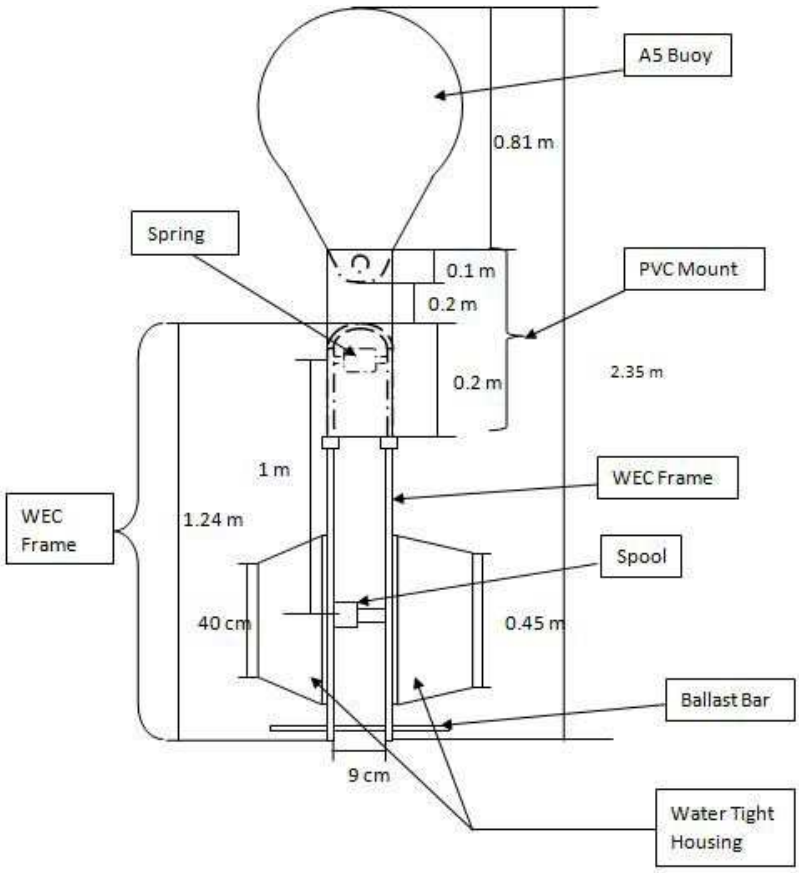

Figure 2.2. The WEC system

The WEC system's PTO is nonlinear and only extracts power when the WEC system's velocity is positive. This PTO has several unique features including a magnetic coupling across an interface window, which allows torque to be transmitted from the wet portion of the device to a completely sealed dry portion containing the generator and associated electronics, Engelmann et al. (2011). A clutch only allows the generator to spin in one direction, and a gear train increases the angular velocity of the generator. A constant pull force spring resets the WEC system for each wave. The WEC system is axi-symmetric and insensitive to wave direction. The design did

not rely on heave resonance (the heave resonance period was 1.1 s). Therefore it was not overly dependent on particular wave frequencies.

2.1 Preparation

Deployment of the WEC system included finding a location and planning the sea trials procedures. The location needed to have an anchor, be safe to dive, wavey, within easy boating range, out of waterways, and cleared by the UH Manoa Dive Safety Office.

2.1.1 WEC System and Drogue

The WEC frame was redesigned from previous experiments to improve the range of the WEC system motion, which affects the functionality of the WEC system. The WEC's motion was limited by two things: spring retract force and allowable travel, or fetch. Spring retract force is the amount of force with which the WEC system's spring retracts the mooring line. The WEC system's spring line and mooring line wrap around two different diameters on the spool. Since the spool is the connection point between the spring and mooring lines, this produces an effective gearing ratio on the spring retract force. The spool allowed the WEC system to move up and down the mooring line as the waves actuated the machine. The spring retract force had to overcome the resistance in the gears and magnets to allow the WEC system to fully reset as each wave passed. The fetch, the distance the spring can extend, is

the distance from the spring to the spool; this limits the amount the WEC generator could rotate. The fetch was extended by increasing the total length of the WEC frame. The WEC frame, spring, and spool are shown in Fig. 2.3. The spring is at the top of the frame and the spool is between the two water-tight casings.

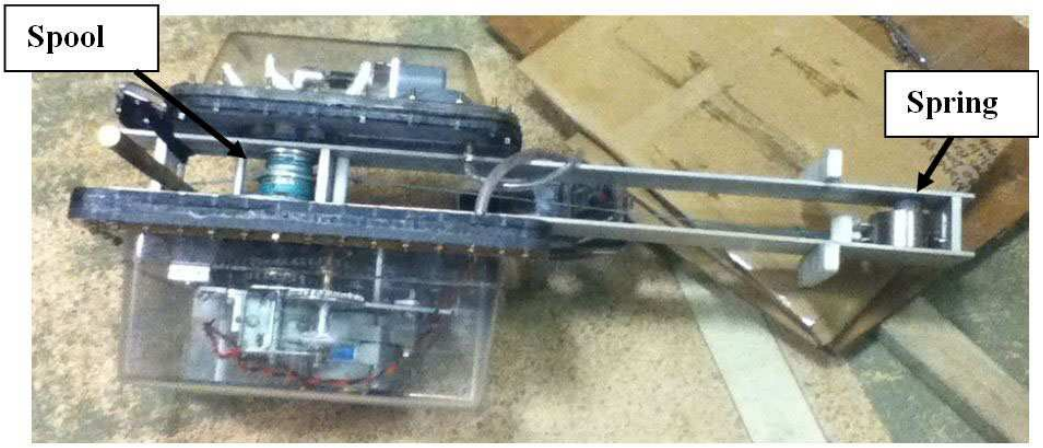

Figure 2.3. WEC frame

There was a need to balance the fetch and spring retract force; with too much fetch, the spring would not be able to retract, but with too little fetch, the spring would slam into the spool, limit power generation, and potentially damage the WEC system. To balance the retract force and the fetch, a spool ratio of 2.5/3 was chosen. This allowed the WEC spring a retract force of 88 N, and a maximum extension length of 1 m; therefore, the WEC system could handle approximately 1.2 m wave height in this configuration. The WEC system would not travel the full wave height because of losses in buoy motion and a delayed heave reaction. A resistor was used as a load for the WEC system during the ocean trials. The resistor was chosen based on the estimated velocity that the WEC system would ride the wave (that corresponds to the

generator RPM), and maximum torque the magnetic couple could take without slip. The power generated at other resistance values found from laboratory test results for the generator, is shown in Fig. 2.4 (Engelmann, 2012).

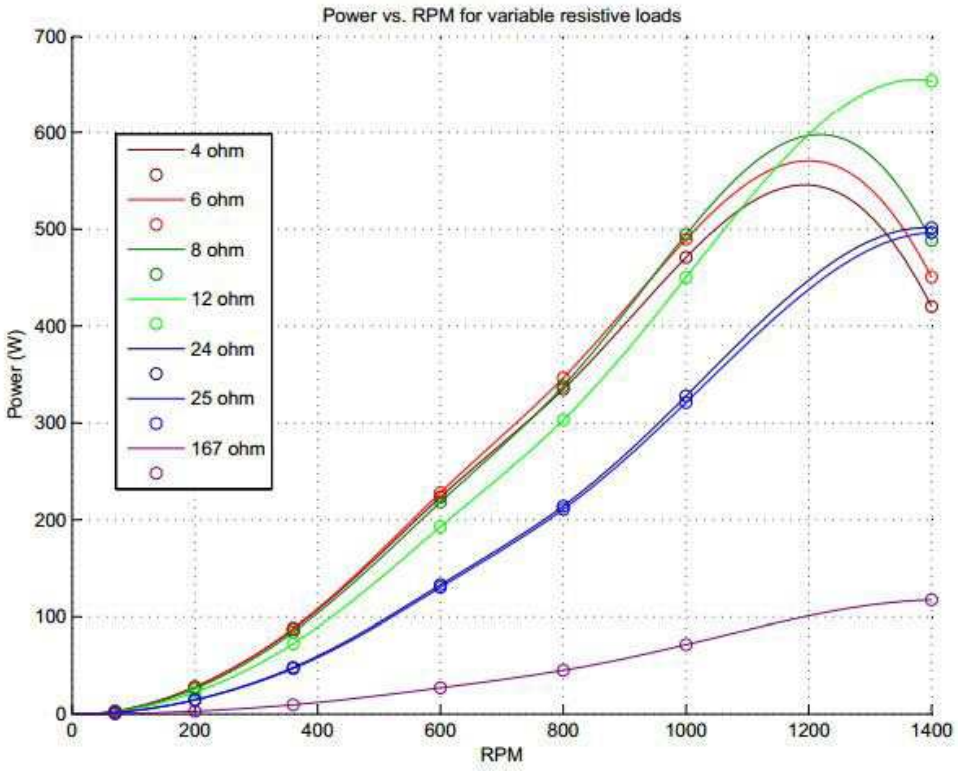

Figure 2.4. Generated Power for a given generator and load

Prior to testing, the buoyancy of the WEC system was calculated to determine the proper ballasting needed for the WEC system to rest vertically (without trim). The bottom of the WEC system needed to be negatively buoyant and hang under the A5 buoy. The net buoyancy of the WEC system was found to be 113 N, with one side being 22 N more buoyant than the other because of different sizes in the water-tight containers. 178 N of standard barbell weight (wet weight of 141 N) were

used to ballast the WEC system. The ballast weights were mounted on the ballast bar that was perpendicular to the machine and bolted down to a plate in the WEC frame as seen in Fig. 2.5 and Fig. 2.2. Ballast weights were arranged to ensure level trim, which allowed for the WEC system to achieve maximum spring extension and power output.

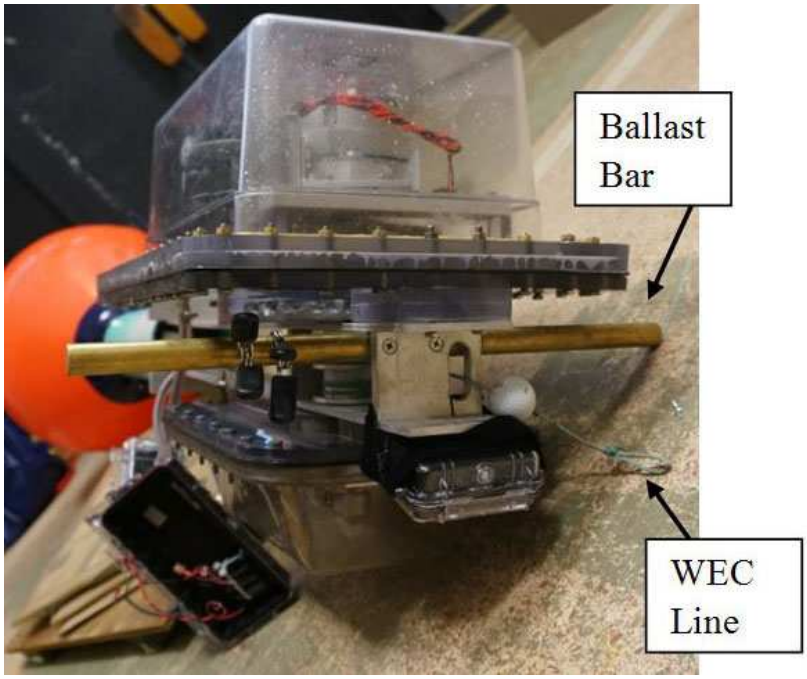

Figure 2.5. Base of the WEC system

The drogue was ballasted to hang vertically under the WEC system and to return to an intended depth if pulled up by the WEC system. It was ballasted by a 27 N rebar top ring, 13 N weight, and chain (weight in air). The drogue had enough negative buoyancy to sink, but not so great to cause the flexible body of the drogue to collapse and lose its frustum form.

To ensure that the bodies would be stable during testing, the center of gravity and

center of buoyancy positions were calculated for each body. The WEC system was approximated with a circular cylindrical shape, and the drogue was approximated by a hollow frustum. For both bodies, the center of gravity was below the center of buoyancy on the same vertical line. The center of gravity and center of buoyancy of both bodies are given in Table 2.1.

	Center of Gravity (m)	Center of Buoyancy (m)
WEC system	-1.369	-1.0782
Drogue	-12.13	-11.192

Table 2.1. Center of gravity and Center of buoyancy of bodies from Still Water Level

Prior to the experiments, the field and dive plans were written to the specifications of the University of Hawai'i at Manoa's Dive Safety Office. The plans described the deployment, recovery and contingency schemes for the ocean trials.

2.1.2 Assembly

The A5 buoy was rigidly attached to the WEC frame with a PVC pipe via a turn-buckle. Two water-tight housings were attached to the WEC frame for the power take-off device and the rotary sensor. The WEC system in Fig. 2.6 was 2.4 m long and weighed 441 N without ballast. Pelican boxes were attached to both water-tight housings for the voltage data loggers.

A ratchet was attached to the WEC line coming from the WEC system. The ratchet held 4.57 m of line that would connect the WEC line at the surface to a loop made in the single-body case mooring line. The ratchet was used to attach the WEC system to the mooring line, as well as to add tension to the mooring line.

Figure 2.6. WEC system assembled

The drogue shape was chosen based on the experiments of Vachon (1975). He observed that the conical drogue moved very little in response to heave, as the connecting lines absorbed much of the heave motion.

The drogue was assembled to a circular rebar frame, which prevented the top ring of the frustum from collapsing and served as ballast weight. The drogue's top straps were tied to a carabiner for connection to the double-body mooring line attached to the WEC system. A ballast weight of 13.3 N (in air), was attached to the bottom to keep the drogue at its full vertical extension. The drogue dimensions are listed in Table 2.2.

	Height (m)	Top Radius (m)	Bottom Radius (m)
Drogue	1.515	0.455	0.063

Table 2.2. Drogue Dimensions

The fully assembled drogue is shown in Fig. 2.7.

Figure 2.7. Assembled Drogue

Mooring lines for the single-body and double-body cases were Amsteel Blue 7/64 line. The line is low-stretch so as not to decrease the efficiency of wave energy capture. This rope exhibits high strength-to-weight ratio, is stronger than a wire rope, and is neutrally buoyant. On the single-body case mooring line, a large carabiner was tied to the end to clip into an eye bolt on the 1.21x1.21x1 m concrete anchor block. A loop was tied at 16.8 m from the mooring side of the rope for the ratchets carabiner. The double-body case mooring line was 8.681 m long and tied to the carabiner that attached to the top of the drogue.

2.1.3 Equipment

The WEC system was prepared for experimentation and data recording by the equipment listed in Table 2.3. The rotary sensor directly measured the heave displacement experienced by the WEC system. The rotary sensor output to a voltage data logger. The Aquadopp measured the total pressure. Linear wave theory was used to obtain the surface elevation of the incoming waves from the Aquadopp data. The Aquadopp was mounted to a frame that rested on the sea floor 1m up-wave in the predominant wave direction from the WEC system. Another voltage logger was connected to the generator and resistive load to measure the voltage over the resistor to calculate the instantaneous power. For this experiment, the load resistor used was 50Ω.

Sensor Equipment	Bits	Accuracy	Rate (Hz)	Measured
Nortek Aquadopp (Nortek AS, 2012)	16	0.5%	1	Depth (m)
Eagletree power logger (Eagletree Systems, 2012)	12	0.5%	10	Voltage (mV)
Madgetech VOLT101A (Madgetech, 2012)	12	0.05%	4	Voltage (mV)
Celesco RT8510 rotary sensor (Celesco, 2012)	16	0.04%	4	Degree

Table 2.3. Sensor Equipment

The rotary sensor and data logger were bench tested separately and together. The rotary sensor came calibrated from the manufacturer. A multimeter and DC voltage generator were used to test the rotary sensor. The DC generator provided power to the rotary sensor and the output voltage was read by the multimeter. The recorded voltage was converted by the factory conversion ratio of volt per degree. The range of motion and sensitivity of the rotary sensor needed to be verified, so the rotary sensor

was spun in multiple increments over the full range, and the distances confirmed.

The voltage data logger was calibrated from the manufacturer and had a program interface to read the recorded data, set sample interval, set the clock, and set start and stop times. The logger was connected to the DC power source, the voltage held for 15 seconds, and then moved to another voltage setting. The logger was confirmed by looking at the recorded data on the computer and comparing it to the known voltage settings.

For the final bench tests, the rotary sensor and voltage data logger were setup to replicate their arrangement during the ocean trials. The rotary sensor was powered by a constructed 27 V battery pack and connected to the voltage data logger inputs. The rotary sensor was rotated a precise distance and the accuracy was checked by looking at recorded change in angular position.

The Aquadopp, rotary sensor, and data logger were synchronized using the National Institute of Standards and Technology (NIST) time. A separate voltage data logger was set to begin recording when input voltage across the resistor was received. The logger's data were used to find the power produced by the WEC system's generator. The rotary sensor's data logger was manually started before the ocean experiments and the rotary sensor continuously output voltage once powered. After the ocean experiment, all sensors were checked for drift over time.

2.2 Experimental Trials

2.2.1 Location

The wave climate at the site was checked to ensure that wave heights would be sufficient to actuate the WEC system during trials. From the recorded data, the site was found to have 0.28 m significant wave height. We used the University's 7.62 m-long boat Kilo Kai to conduct the experiments. GPS points were taken of the anchor block for the single-body case, and of the start as well as the end location for the double-body case. The site bathymetry and anchor location are shown in Fig. 2.8 (Pawlak, 2012).

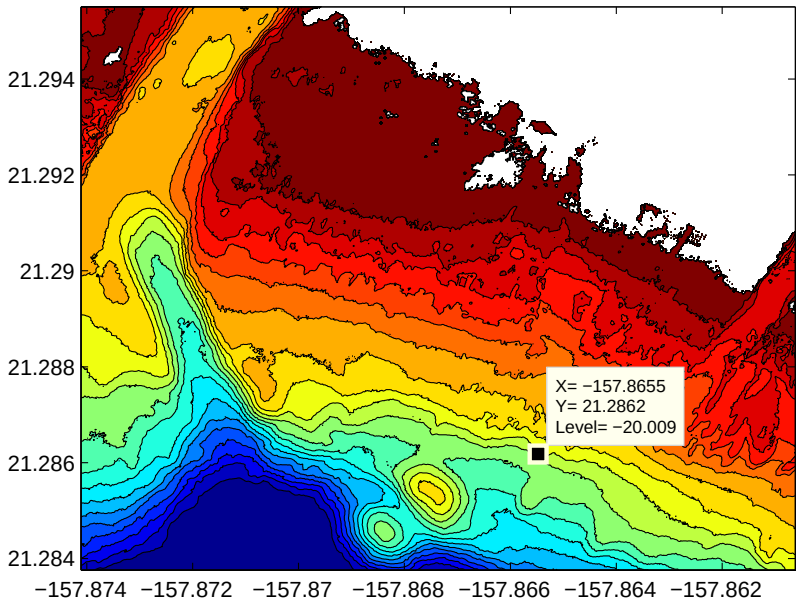

Figure 2.8. Site bathymetry and anchor location

2.2.2 Single-Body Case

Before testing, a tag line was attached to the WEC system, and the ratchet was clipped onto the WEC line. The WEC system was lowered into the water, where divers took the extended portion of the ratchet and clipped the carabiner to the loop on the mooring line. The divers ratcheted up the excess line to create a taut mooring, but care was taken not to cause any extension in the WEC system's spring. This allowed the WEC system to be held securely in place and to achieve full range of extension. The WEC system during the trials is shown in Fig. 2.9.

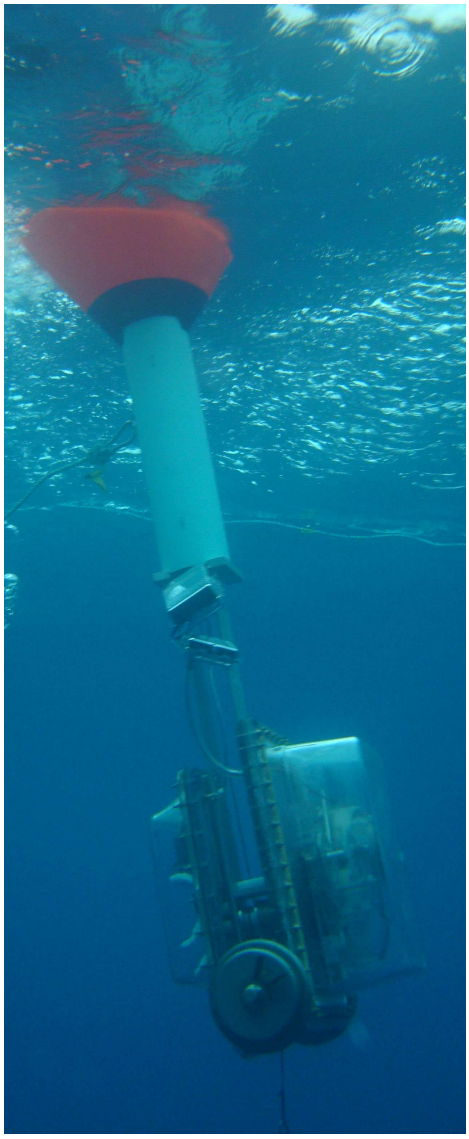

Figure 2.9. WEC system during trial

During the single-body case, wave conditions were about 0.2 m swell height with periods of 15-16 s; however, shorter wind waves and boat wakes sometimes provided larger waves at random times. The WEC system was allowed to run undisturbed for two hours in about 20 m of water.

2.2.3 Double-Body Case

The WEC system was pulled to the side of boat and the double-body case mooring line clipped onto the WEC line. The single-body case mooring line and ratchet were unclipped and the drogue tossed overboard and allowed to sink naturally. It was checked that the drogue was extended and was directly below the WEC system. A tag line was left on the freely floating WEC system for control in case it drifted into boat traffic or too close to shore. The WEC system floated in 16-19 m of water. The double-body was similar to the single-body case except that there was no ratchet, and that the mooring line connected directly to the WEC system.

CHAPTER 3

NUMERICAL MODELING

3.1 Problem Description

3.1.1 Simplifications and Assumptions

It is assumed that the fluid is inviscid and incompressible and the flow is irrotational. The WEC system (Body A) and drogue (Body B) are considered rigid bodies that only act in one degree of freedom (heave) due to the external heave forces. Therefore, the double-body case will experience two degrees of freedom, one for each body. The two bodies are far enough apart to not hydrodynamically interact, so the only interaction between the two bodies is through the cable that connects them. The bodies are axi-symmetric and are not affected by waves incident from different directions; therefore, the coordinate systems will always align with the direction of the incoming wave propagation.

3.1.2 Coordinate System

Two coordinate systems are defined in this work. Their origins are at the center of gravity of each body, with the x-axis pointing to the right, the y-axis pointing into the paper, and the z-axis pointing up vertically. A two body-coordinate systems exist in the double-body case. Body A, the WEC system, is the body that pierces the free surface and its body-coordinate system is represented by A. Body B, the submerged

drogue, is represented by B. For the single-body case, the body-coordinate system is the same as Body A. The irregular surface elevation is calculated with respect to the horizontal position of the center of gravity of Body A. All body accelerations, velocities, displacements, and complex force transfer functions are taken with respect to the center of the body coordinate system.

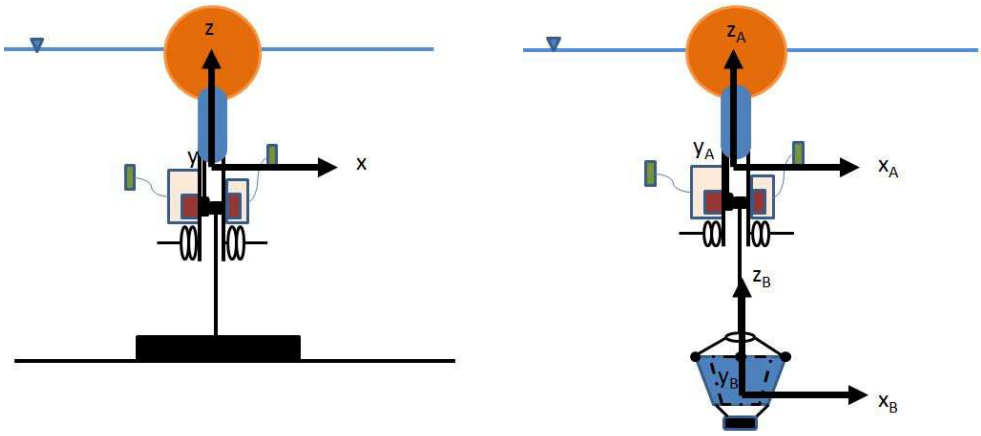

Figure 3.1. Coordinate system

3.1.3 Review of Potential Theory

The problem of a body's interaction with waves can be solved by means of linear potential theory and through a series of boundary-value problems. Assuming small-amplitude progressive waves and correspondingly small motions of a body with no forward speed, the total velocity potential is the sum of the incident potential, diffraction potential, and radiation potential. The total velocity potential, ϕ, can be written as

$$\phi = \phi_0 + \phi_7 + \sum_{j=1}^{6} \phi_j, \tag{3.1}$$

where ϕ_0 is the incident potential, ϕ_7 is the diffraction potential, and ϕ_j is the radiation potential for $j = 1, ..., 6$ degrees of motion. The incident potential represents the potential of the incoming waves with no body present. The diffraction potential represents the potential of diffracted waves acting on a body that is fixed. The radiation potential is the potential when the body oscillates within prescribed motions in an otherwise calm fluid.

All potentials $(\phi_0, ..., \phi_7)$ must satisfy Laplace's equation

$$\nabla^2 \phi_j = 0, \text{ in the fluid domain,} \tag{3.2}$$

and the boundary conditions,

$$\frac{\partial^2 \phi_j}{\partial t^2} + g\frac{\partial \phi_j}{\partial z} = 0, \text{ the still water surface,} \tag{3.3}$$

$$\frac{\partial \phi_0}{\partial n} = -\frac{\partial \phi_7}{\partial n}, \text{ on fixed body or surface,} \tag{3.4}$$

$$\frac{\partial \phi_7}{\partial n} = 0, \text{ on fixed seafloor,} \tag{3.5}$$

where n is the unit normal vector directed into the body, z is the vertical coordinate, t is time, and g is the acceleration due to gravity.

In addition to these conditions, the radiation and diffraction potentials must also satisfy the radiation condition:

$$\lim_{R\to\infty} \sqrt{R}(\frac{\partial}{\partial R} + ik)\phi_j = 0, \tag{3.6}$$

for $j = 1, ..., 7$, where R is the radial distance from the center of the body and k is the wave number.

Once all potentials are known through the use of the Green-function method, Euler's integral can be used to determine the pressures, and thus, to calculate the Froude-Krylov force, diffraction force, added mass and damping coefficients.

3.2 Sea Surface Calculation

In this study, the body's (bodies') response to irregular seas is calculated for different wave spectra. A Bretschneider spectrum is used to model the desired seas. The Bretschneider spectrum is given by

$$\begin{aligned} S(\sigma_i) &= (A/\sigma_i^5)exp(-B/\sigma_i^4), \\ A &= (5/16)\sigma_n^4 H_s^2, \\ B &= (5/4)\sigma_n^4, \end{aligned} \tag{3.7}$$

- σ_n is the peak frequency of the desired wave spectrum as a function of the angular frequency (rad/s)
- H_s is the significant wave height of the desired the wave spectrum (m)
- σ_i is the angular frequency of the spectrum

The irregular sea surface is generated by the summation of a finite number of sinusoidal waves. The amplitudes of the component waves are determined from the wave spectrum, and random phase angles from 0 to 2π. The sea surface elevation simulated at the center of gravity of Body A can be written as

$$\eta(t) = \sum_{i=1}^{N} A_i cos(\sigma_i t - \epsilon_i). \tag{3.8}$$

- A_i is the amplitude of the i-th wave component:

$$A_i = \sqrt{2S(\sigma_i)\Delta\sigma_i} \tag{3.9}$$

- σ_i is the frequency (rad/s) of the i-th component
- ϵ_i is the random phase angle of the i-th component, uniformly distributed between 0 to 2π
- N is the number of wave components
- $\Delta\sigma_i$ is the frequency interval
- t is the time.

3.3 Equations of Motion

The equations of motion express the motion of a body in terms of the external forces, mass, damping and restoring properties. The equations of motion are found by summing all the forces acting on the body, then applying Newton's second law. Newton's second law is given by

$$\sum F = m\ddot{z}, \tag{3.10}$$

where m is the mass matrix, $\ddot{z}$ is the body acceleration, and $\sum F$ is the sum of all the forces acting on the system. The sum of forces acting on a body in this study is given by

$$\sum F = F_m + F_{hs} + W + F_R + F_{wec} + F_{W_k} + F_{VD}, \tag{3.11}$$

where

- F_m is the mooring force resulting from the mooring line; or in the double-body case, the force acting on the cable connecting the WEC system and drogue:

$$F_m = -K_m z(t) \tag{3.12}$$

- F_{hs} is the hydrostatic force resulting from buoyancy. It is composed of two parts, initial and dynamic. The initial is the static buoyancy force acting on the object with no waves present and is a constant upward force equal to the weight of water displaced, Δ. The dynamic part represents the change in hydrostatic force as the body moves up and down in the waves:

$$F_{hs} = F_{hs_o} - F_{hs_d} = \Delta - \rho g A_w z(t) \tag{3.13}$$

- F_{wec} is the force resulting from the PTO. In this work, the force is caused by a generator and spring. The spring is a constant pull force spring, which supplies a constant force unrelated to its deflection (Ming Tai Industrial Co, 2012). The spring is represented by $F_{constant}$. The generator is represented by a viscous dashpot damper, C_{DD}, as power generation dampens the WEC motion. Keller (2011) measured the C_{DD} of one PTO in Phase 2 as $981.14\frac{Ns}{m}$. The C_{DD} was calculated by:

$$C_{DD} = \frac{\text{pull force}}{\text{winding velocity}} \tag{3.14}$$

In the numerical model, a range of C_{DD} values is evaluated to simulate different PTOs or multiple PTOs on the WEC system. The power generation and C_{DD}

can only occur when the WEC system has a positive upward velocity or, in the double-body case, has a positive relative velocity. This characteristic is represented by the Heaviside function $H(\dot{z}(t))$. It should be noted that C_{DD} will increase or decrease based on the load resistance.

$$F_{wec} = -C_{DD}\dot{z}(t)H(\dot{z}(t)) - F_{constant} \tag{3.15}$$

- F_R represents the hydrodynamic radiation forces. The radiation forces consist of the added mass and wave damping forces. The added mass force is the force it takes to move the body through the water. The damping force is the force on the body when it makes its own waves. The added mass, a, and damping , b, are frequency dependent. The transformation of the forces to the time domain is discussed in later sections. The radiation force is

$$F_R = -a(\sigma)\ddot{z} - b(\sigma)\dot{z} \tag{3.16}$$

- F_{W_k} represents the vertical components of the wave exciting forces. The wave exciting forces are the summation of the incoming and diffracting forces.

- W represents the body's weight, which is constant.

$$W = -constant \tag{3.17}$$

- F_{VD} is the vertical viscous drag force given by

$$F_{VD} = \frac{1}{2}C_D\rho A_p(wv - \dot{z}(t))|(wv - \dot{z}(t))| \tag{3.18}$$

where C_D is the vertical drag coefficient, A_p is the projected area, wv is the vertical water particle velocity, and $\dot{z}(t)$ is the body vertical velocity. The WEC system or Body A have a shape similar to a circular cylinder, which does not have a large projected area as a it moves in heave (small viscous effects). Therefore, for preliminary modeling, the vertical viscous drag force was considered negligible. Model comparisons with experimental tests show good agreement without the addition of the viscous drag force; therefore, the viscous drag force for Body A and the WEC system are ignored. If viscous drag force for Body A body is included body motions and power will be slightly reduced from the case with no viscous drag on Body A. The viscous drag for Body B is not negligible, and is included in the calculations. Vachon (1973) and Holler (1985) performed tow-tank tests to measure the drag coefficient for different drogues. The tension and angle of the towing cable were measured by a load cell and rotary variable differential transformers. The vertical drag force of the drogue, $F_V D = T sin\theta$, is calculated where T is the tension of the towing line and θ is the angle of the towing line. The drag coefficient was then found from

$$F_{VD} = \frac{\rho}{2} C_D A_p V^2, \tag{3.19}$$

where A_p is the projected area, V is the relative velocity, ρ is water density, and C_D is the drag coefficient. The drag coefficient of a conical drogue is based on the projected area of the drogue, $A_p = \pi(D^2 - d^2)/4$.

It should be noted that $\ddot{z}(t)$, $\dot{z}(t)$, and $z(t)$ represent the body acceleration, velocity, and displacement, respectively. Free body diagrams (FBD) were made for each case; as a result, the sum of forces can be simplified for each case. This is done in later sections.

3.3.1 Diffraction and Froude-Krylov Forces

Three-dimensional mesh models were created in MATLAB, for the WEC system and drogue. These meshes were constructed out of triangular and rectangular panels. The drogue consisted of 572 panels, and the WEC system consisted of 400 panels. This number of panels is satisfactory since higher order potential forces are not considered. The WEC system mesh is not exactly the same as the ocean tested prototype. The main difference is the elliptical cylinder bottom. To ensure accurate results, the bottom surface area is made equivalent to the bottom surface area of the prototype. The meshes were run in HYDRAN (2008), which uses the Green-function method to obtain the frequency domain complex transfer functions $H^D(\sigma)$ and $H^{FK}(\sigma)$ for the diffraction and Froude-Krylov forces, respectively, for each body. The summation of these forces is the wave exciting forces. The mesh models are shown in Figs. 3.2 and 3.3.

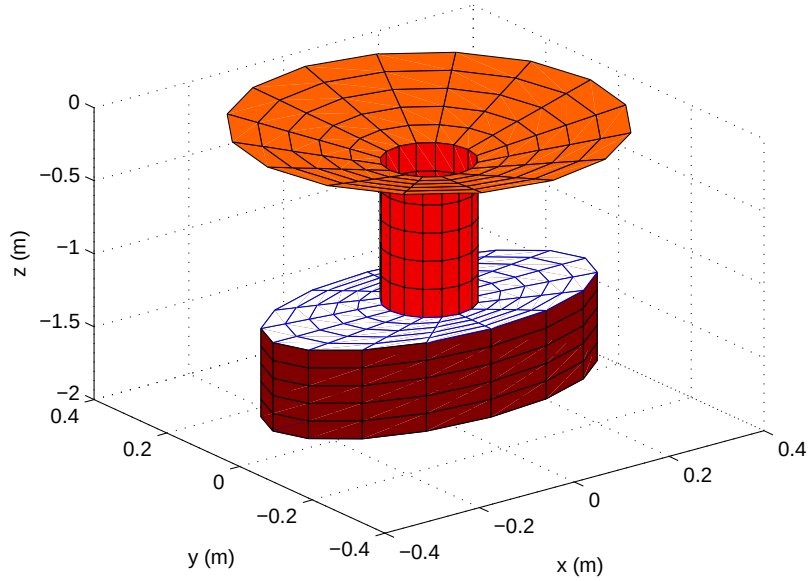

Figure 3.2. Three-dimensional WEC system mesh

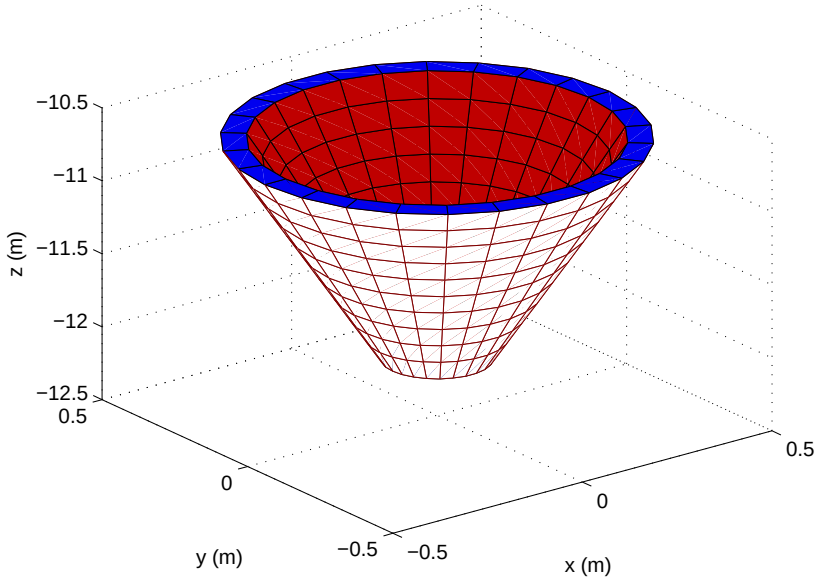

Figure 3.3. Three-dimensional drogue mesh

The diffraction or scattering transfer function is given as

$$H^D(\sigma) = F^D(\sigma)/A(\sigma) \tag{3.20}$$

where $F^D(\sigma)$ is the complex diffraction force for the frequency σ, and $A(\sigma)$ is the corresponding wave amplitude found by the irregular sea surface spectrum. To find the diffraction force in the time domain, the Fourier transform of $F^D(\sigma)$ is taken and the convolution theorem applied, see e.g., Otto de Kat, (1988). It is assumed that the wave motion has been going on for a long time, allowing the transient effects to die out, and the wave process is stationary. Therefore, the time dependent linear diffraction force can be expressed in terms of the transfer function for the regular wave condition:

$$F^D(t) = A(\sigma)H^D(\sigma)e^{i(\sigma t-\epsilon)}. \tag{3.21}$$

Equation (3.21) can be rewritten for $H^D(\sigma)$ in terms of its real, $HR^D(\sigma)$, and imaginary parts, $iHI^D(\sigma)$, and the exponent in terms of *sin* and *cos* functions:

$$F^D(t) \;=\; A(\sigma)\{HR^D(\sigma) + iHI^D(\sigma)\}\{cos(\sigma t - \epsilon) + isin(\sigma t - \epsilon)\} \tag{3.22}$$

Only the real part of Eq. (3.22) has a physical meaning. Therefore, the equation for the diffraction force in the time domain can be written as (see e.g., Chitrapu (1992))

$$F^D(t) = \sum A(\sigma)(HR^D(\sigma)cos(\sigma t - \epsilon) - HI^D(\sigma)sin(\sigma t - \epsilon)) \tag{3.23}$$

The Froude-Krylov forces, due to the incident wave pressure, can be obtained using a similar method. The Froude-Krylov force transfer function is, $H^{FK}(\sigma)$, and $A(\sigma)$

is the corresponding wave amplitude found by the irregular sea surface calculation. This gives the complex Froude-Krylov force:

$$F^{FK}(t) = A(\sigma)H^{FK}(\sigma)e^{i(\sigma t-\epsilon)} \tag{3.24}$$

The same assumptions and methods to find the diffraction force are made to obtain the real part of the Froude-Krylov force in the time domain:

$$F^{FK}(t) = \sum A(\sigma)(HR^{FK}(\sigma)cos(\sigma t-\epsilon) - HI^{FK}(\sigma)sin(\sigma t-\epsilon)). \tag{3.25}$$

The wave exciting forces are the summation of the Froude-Krylov and diffraction forces for each time t.

3.3.2 Radiation Force

The hydrodynamic radiation forces are calculated in the frequency domain and converted to the time domain using the theory of Cummins' (1962). He studied the hydrodynamic problem of an ideal fluid in the time-domain, to find a representation for the linear pressure forces. Ogilvie (1964) proved the relationship between the frequency dependent added mass and damping to the time domain using the Fourier Transform theory. From their work, the following expressions relating the frequency

dependent hydrodynamic coefficients to the time domain coefficients can be written:

$$\begin{aligned} a(\sigma_1) &= A_{33} - \frac{1}{\sigma_1}\int_0^\infty K(\tau)sin(\sigma_1\tau)d\tau \\ A_{33} &= a(\sigma_1) + \frac{1}{\sigma_1}\int_0^\infty K(\tau)sin(\sigma_1\tau)d\tau \\ b(\sigma) &= \int_0^\infty K(\tau)cos(\sigma\tau)d\tau \\ K(\tau) &= \frac{2}{\pi}\int_0^\infty b(\sigma)cos(\sigma\tau)d\sigma \end{aligned} \tag{3.26}$$

where

- A_{33} is the genuine added mass or $a(\infty)$
- a is the frequency dependent added mass
- τ is time lag
- σ_1 is a specific frequency where the frequency dependent added mass is known
- $K(\tau)$ is the Kernel or retardation function
- b is the frequency dependent radiation damping

Given Eq. (3.26) and (3.16), it is now possible to solve for the radiation forces acting on the body due to small arbitrary motions in the time domain. The radiation force on a body is written as

$$F_R = -A_{33}\ddot{z}(t) - \int_0^t K(\tau)\dot{z}(t-\tau)d\tau \tag{3.27}$$

The first term in Eq. (3.27) represents the forces due the acceleration of the structure. The second term represents the fluid memory effect that incorporates the energy dissipation due the radiated waves caused by the motion of the structure.

3.3.3 Single-Body Case

The equations of motion in the time domain for the single-body case represent a moored, surface piercing buoy as seen in the free-body diagram (FBD) in Fig. 3.4.

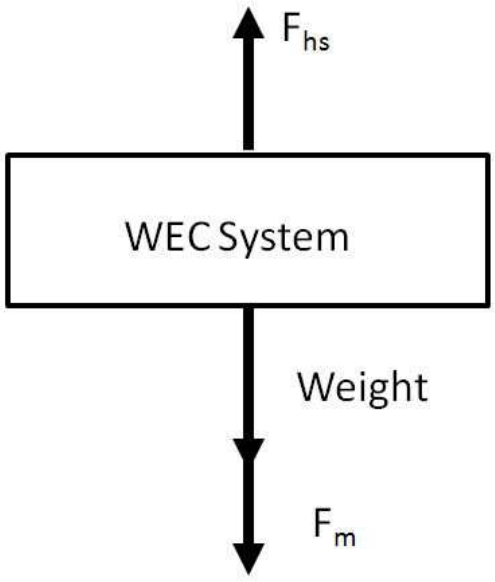

Figure 3.4. External static FBD on WEC system

The sum of the static external forces, shown in Fig. 3.4, can be written as

$$\sum F = F_{hs} - W - F_m \tag{3.28}$$

The internal static FBD of Fig. 3.5 shows that the WEC's constant pull force spring, $F_{constant}$, is a fraction of the mooring force:

$$F_m = \alpha F_{constant} \tag{3.29}$$

where α is the ratio of the two diameters of the spool.

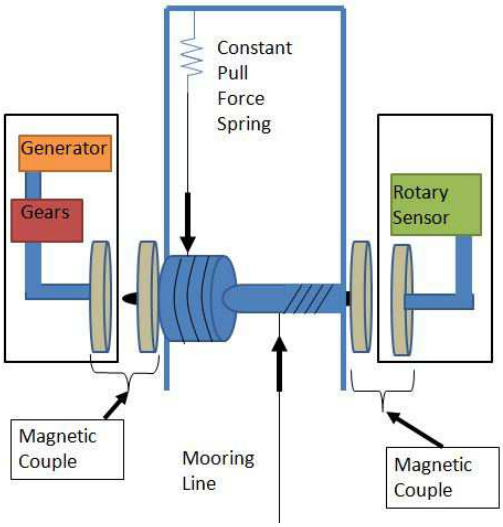

Figure 3.5. Internal static FBD of the WEC system

The internal dynamic FBD, Fig. 3.6, shows that $F_{constant}$, and the torque of the WEC's generator are equal to the mooring force when the buoy is moving.

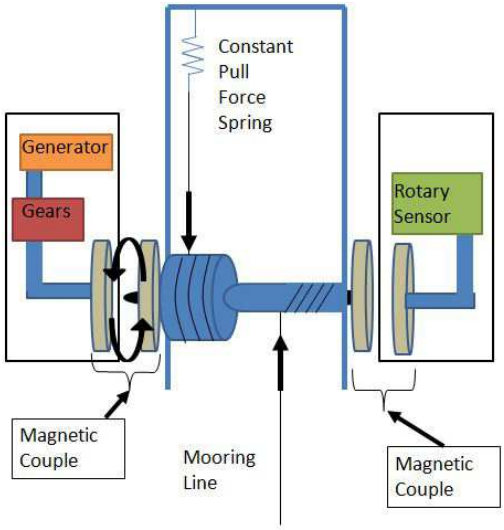

Figure 3.6. Internal dynamic FBD on WEC system

The circular arrows in Fig. 3.6 show the generator's applied torque to the system(over

half the wave cycle). The generator's torque is

$$Tor = C_\theta \dot{\theta},$$

where C_θ is the angular momentum and $\dot{\theta}$ is the angular velocity. This rotational force is translated into a vertical force. The angular velocity is related to the vertical velocity by

$$\dot{z} = r_{morr}\dot{\theta},$$

where r_{morr} is the radius of the spool connected to the mooring line. The torque, or moment, is rewritten in terms of a vertical force, F_{gen}, and the radius of the spool connected to the generator, r_{spool},

$$F_{gen} r_{spool} = Tor.$$

As a result the linear force of the generator is written as,

$$F_{gen}(t) = \frac{C_\theta}{r_{spool} r_{morr}} \dot{z}(t) = C_{DD}\dot{z}(t).$$

Therefore F_m is given by

$$F_m = \alpha F_{constant} + C_{DD}\dot{z}(t)H(\dot{z}(t)). \tag{3.30}$$

To find the equations of motion, Eq. (3.10), (3.13), and (3.30) are substituted into Eq. (3.28) to obtain

$$m\ddot{z} = \nabla - \rho g A_w z(t) - W - \alpha F_{constant} - C_{DD}\dot{z}(t)H(\dot{z}(t)).$$

Fig. 3.4 shows that the weight and static mooring force cancel with the initial hydrostatic force giving

$$m\ddot{z} = -\rho g A_w z(t) - C_{DD}\dot{z}(t)H(\dot{z}(t)).$$

The external dynamic forces, the radiation and wave exciting forces, are now added:

$$m\ddot{z} = -\rho g A_w z(t) - C_{DD}\dot{z}(t)H(\dot{z}(t)) + F_R + F_{W_k} \tag{3.31}$$

Finally, by substituting Eq. (3.27), into Eq. (3.31), and adding like terms, the single-body case equations of motion becomes

$$(m + A_{33})\ddot{z}(t) + \int_0^{\tau_{max}} K(\tau)\dot{z}(t-\tau)d\tau + C_{DD}\dot{z}(t)H(\dot{z}(t) + \rho g A_w z(t) = F_{W_k} \tag{3.32}$$

3.3.4 Double-Body Case

The equations of motion for the double-body case represent a freely floating two body system, with Body A piercing the free surface and Body B fully submerged and ballasted. The double-body case has two equations of motion, one for each body. Body A's equations of motion, was found to be similar to the single-body case, except that the velocity is the relative velocity of the two bodies. The equation of motion for Body A is given by

$$(m^A + A^A_{33})\ddot{z^A}(t) + \int_0^{\tau_{max}} K^A(\tau)\dot{z}^A(t-\tau)d\tau +$$
$$C_{DD}\dot{z_{rel}}(t)H(\dot{z_{rel}}(t)) + \rho g A^A_w z^A(t) = F^A_{W_k}, \quad (3.33)$$

where $\dot{z}_{rel} = (\dot{z}^A(t) - \dot{z}^B(t))$ is the relative velocity between Body A and Body B.

Body B is attached to Body A by a cable, and is supposed to remain relatively motionless to act as a floating anchor point for Body A. The drogue should allow the WEC system's PTO to work approximately the same as when moored to the sea floor. The drogue's FBD is shown in Fig. 3.7.

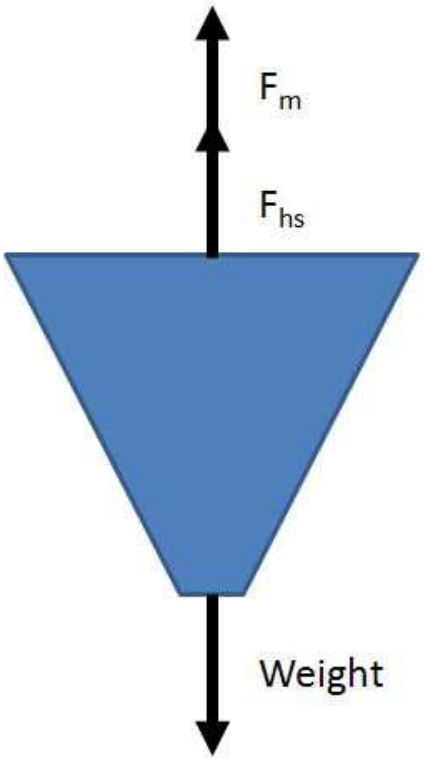

Figure 3.7. External static FBD of the drogue

From the diagram, the sum of static external forces is:

$$\sum F = F_{hs}^{B} - W^{B} + F_{m} \tag{3.34}$$

As in the single-body case, Eq. (3.10), Eq. (3.13), and Eq. (3.30) can be substituted into Eq. (3.34) to obtain

$$m^{B}\ddot{z}^{B} = F_{hs_o}^{B} - F_{hs_d}^{B} - W^{B} + \alpha F_{constant} + C_{DD}\dot{z_{rel}}(t)H(\dot{z_{rel}}(t)) \tag{3.35}$$

The external dynamic forces, the radiation, viscous drag, and wave exciting forces, are added to obtain:

$$m^{B}\ddot{z}^{B} = F_{hs_o}^{B} - F_{hs_d}^{B} - W^{B} + \alpha F_{constant} + C_{DD}\dot{z_{rel}}(t)H(\dot{z_{rel}}(t)) + F_{R}^{B} + F_{W_k}^{B} + F_{VD}^{B} \tag{3.36}$$

Because Body B is fully submerged, the hydrostatic force, F_{hs_d}, is zero. The drogue is far from the free surface, and therefore, the hydrodynamic radiation damping is also zero. HYDRAN (2008) confirmed that the radiation damping is zero.

The equations of motion of Body B are now written as

$$(m^{B} + A_{33}^{B})\ddot{z}(t) - F_{hs_o}^{B} + F_{hs_d}^{B} + W^{B} - \alpha F_{constant} - C_{DD}\dot{z}_{rel}(t)H(\dot{z}_{rel}(t)) - F_{VD}^{B} = F_{W_k}^{B} \tag{3.37}$$

Similar to Body A, Eq. (3.34) shows that the weight of the drogue is equal to the initial hydrostatic force and the mooring force. However, these forces cannot be canceled as in Body A because of conditions set on the connecting line:

1. If $z_{rel} < 0$ then the connecting cable is slack and no power can be generated (Body A and Body B act as single bodies). Therefore $F_m = \alpha F_{constant} +$

$C_{DD}\dot{z}_{rel} = 0$ ($\alpha F_{constant} = 0$ and $C_{DD} = 0$). This occurs when Body B's displacement is greater than Body A.

2. If $z_{rel} > 0$ then the connecting cable is taut. This only means that the static mooring, $F_m = \alpha F_{constant}$ is acting on the system. This occurs only when Body A has a larger positive displacement than Body B. The displacements are relative to the respective bodies' initial starting position designated by the initial conditions.

3. If $\dot{z}_{rel} > 0$ and $z_{rel} > 0$ then it is possible for the PTO to capture wave energy (C_{DD} and $\alpha F_{constant}$ forces are acting on the system). $\dot{z}_{rel} > 0$ occurs when Body A's velocity is greater than Body B. The maximum relative velocity is when Body A has a positive velocity and Body B has a negative velocity. This can cause jerks on the line. On the other hand, if $\dot{z}_{rel} < 0$ then $C_{DD} = 0$ and the PTO will not produce power. This arises when Body A's velocity is less than Body B's velocity.

To remove improbable data, a tolerance was set for $\dot{z}_{rel}$ and z_{rel}, 0.001m/s and 0.001m, respectively. Therefore if power was predicted for a relative displacement or velocity under 0.001, the power is set to zero at that time. This is done after solving for the equations of motion. The tolerance removes many of the random power spikes that are unlikely events, such as 45W of power produced with a 0.5mm relative displacement that the model would produce without the use of such tolerance.

In summary, before the equations of motion, namely Eqs. (3.33) and (3.37) can be solved, the bodies' respective velocities and displacements must be determined at time t. The relative displacement, z_{rel}, determines the condition of the connecting cable (taut or slack), and the relative velocity, $\dot{z}_{rel}$, determines the condition of the PTO (generating power or not generating power).

3.4 Solving the Equations of Motion

3.4.1 Evaluation of the Radiation Kernels

HYDRAN (2008) calculates the frequency dependent added mass and damping coefficients for a range of frequencies. The difficulty in solving for damping is the numerical integration of the Kernels in Eq. (3.26), and it is due to the oscillatory nature of the integrand for high values of τ. Trapezoidal and Simpson's rules for numerical integration require closely spaced intervals and take a very long computational time. Therefore, Filon's method, which is used to solve integrals in the form

$$\int_a^b f(x)cos(kn)dx \quad \text{and} \int_a^b f(x)sin(kn)dx \tag{3.38}$$

was used to solve

$$K(\tau) = \int_0^{\sigma_f} b(\sigma)cos(\sigma\tau)d\sigma \tag{3.39}$$

where σ_f is the max frequency where $b(\sigma)$ becomes zero. The basic methodology of Filon's method is that the function $f(x)$ is smooth over the interval (a,b) and can be approximated by a polynomial so that the integration over the sub-intervals is performed analytically. The entire integration can be approximated by the summation

of discrete integrals over the sub-intervals. Full details of Filon's method are given in Otto de Kat (1988).

3.4.1.1 Numerically Solving the Memory Integral

With the frequency independent added mass and kernel functions found in the previous section, the memory effect integrals in Equations (3.32) and (3.33) need to be evaluated. The memory effect integral for the single-body case is written as

$$M(t) = \int_0^\infty K(\tau)\dot{z}(t-\tau)d\tau, \tag{3.40}$$

where $K(\tau)$ is the Kernel function and $\dot{z}$ is the velocity of the center of gravity of the body. The upper limit of the memory effect integral can be replaced by τ_{max}, which is the time were $K(\tau)$ reaches a constant value. In this study, a value of 30 s is selected for τ_{max}. The time interval of $\nabla\tau$ was chosen the same as the interval of the numerical integration, ∇t. This allows the time history of velocity and the Kernel functions to be specified at the same time intervals. A value of $\nabla t = \nabla\tau = 0.2s$ has been chosen in this study. A trapezoidal integration scheme is used to evaluate the memory intervals. It should be noted, that when $t \leq \tau$, velocity is equal to zero.

3.4.1.2 Rewriting the Equations of motion

To solve the equations of motion, Eqs. (3.32), (3.33), and (3.37) are first rewritten in the form of a 1^{st}-order ordinary differential equation (ODE) such as

$$\frac{dv}{dt} = f(t, v). \tag{3.41}$$

This 1^{st}-order ODE can be solved if the initial conditions for all the variables are known using a standard numerical method, such as 4^{th}-order Runge Kutta or Modified Euler method. In general, to solve an ODE, the right hand side of Eq. (3.41) is evaluated one or more times at each time step to find the extrapolation of the solution at the next time step. The equations of motion for the bodies in this paper contain unknowns and also the derivatives of the unknowns on the right hand side of the equation. The equations of motion need to be rewritten such that the right hand side does not include accelerations. The forces that do not depend on accelerations can be grouped into the term F_o. The general procedure is the same for all of the bodies, so only the single-body case is described here. To rearrange Eq. (3.32) into the Eq. (3.41), all forces independent of acceleration are grouped in a term F_o

$$F_o = -\int_0^{\tau_{max}} K(t-\tau)\dot{z}(\tau)d\tau - C_{DD}\dot{z}(t)H(\dot{z}(t)) - F_{hs_d}z(t) + F_{W_k}.$$

As a result, the equation can be written as

$$(m + A_{33})\ddot{z}(t) = F_o. \tag{3.42}$$

Dividing by the total mass, the equation becomes

$$\ddot{z}(t) = F_o(m + A_{33})^{-1}, \tag{3.43}$$

or it can be written as two coupled ODEs, one for the position, z, and one for the velocity, $\dot{z}(t)$:

$$\begin{aligned} \frac{d\dot{z}(t)}{dt} &= f(\dot{z}(t), z(t), t), \\ \frac{dz(t)}{dt} &= \dot{z}(t). \end{aligned} \tag{3.44}$$

3.4.2 Numerically Solving the Coupled ODEs

For this study, the 4^{th}-order Runge Kutta method is used to evaluate the coupled 1^{st}-order ODEs of velocity and displacement in Eq. (3.44). For the double-body case, four 1^{st}-order ODEs are needed (two for each body). The initial velocities and displacements of all bodies are set to zero. For the single-body case, the 4^{th}-order Runge Kutta method can be written as

$$
\begin{aligned}
s(t,1) &= \Delta t f(t, \dot{z}(t), z(t)) \\
d(t,1) &= \Delta t f(t, \dot{z}(t)) \\
s(t,2) &= \Delta t f(t + \frac{\Delta t}{2}, \dot{z}(t) + \frac{s(t,1)}{2}, z(t) + \frac{d(t,1)}{2}) \\
d(t,2) &= \Delta t f(t + \frac{\Delta t}{2}, \dot{z}(t) + \frac{s(t,1)}{2}) \\
s(t,3) &= \Delta t f(t + \frac{\Delta t}{2}, \dot{z}(t) + \frac{s(t,2)}{2}, z(t) + \frac{d(t,2)}{2}) \\
d(t,3) &= \Delta t f(t + \frac{\Delta t}{2}, \dot{z}(t) + \frac{s(t,2)}{2}) \\
s(t,4) &= \Delta t f(t + \Delta t, \dot{z}(t) + s(t,3), z(t) + d(t,3)) \\
d(t,4) &= \Delta t f(t + \Delta t, \dot{z}(t) + s(t,3))
\end{aligned} \tag{3.45}
$$

$$
\begin{aligned}
\dot{z}(t + \Delta t) &= \dot{z}(t) + \frac{1}{6}[s(t,1) + 2s(t,2) + 2s(t,3) + s(4)] \\
z(t + \Delta t) &= z(t) + \frac{1}{6}[d(t,1) + 2d(t,2) + 2d(t,3) + d(4)]
\end{aligned} \tag{3.46}
$$

The right hand side of Eq. (3.44) is evaluated 4 times at each step as shown in Eq. (3.45). The initial forces are determined from the user defined body's initial conditions. The initial forces are then summed to obtain the total force acting on the body, thus F_o, m, and A_{33} are known for the body's initial conditions. This solves the right hand side of Eq. (3.43), which is used to evaluate s(1) and d(1) in Eq. (3.45). The body's motion is updated with the value of s(1) and d(1)and the forces are computed again with the updated values to calculate s(2) and d(2). This is repeated to get s(3), s(4), d(3), and d(4). The body's motions for the next time step are obtained with Eq. (3.46). Please note that the memory effect integrals in Eq.

(3.40) are evaluated by the trapezoidal method four times at each time step (once for s(1),...s(4)).

In the double-body case, the bodies are coupled, or the motion of Body A depends on the motion of Body B and vice versa. Therefore, the equations of motion for both bodies are solved simultaneously for each body's velocity and displacement. The 4^{th}-order Runge Kutta method of solution is similar to the single-body case, except that conditions are set at each half step to determine if the connecting line is slack or taut and if the PTO is generating power (the conditions are listed in Section 3.3.4).

Using initial conditions, the state of the connecting cable and PTO are determined, and the equations of motions are solved for the first step in the 4^{th}-order Runge Kutta method. The velocities and displacements are updated to solve over the next half time step. This is repeated four times at each time t, then the bodies' motions for the next time step are obtained with Eq. (3.46).

Because of the high-order of the 4^{th}-order Runge Kutta method used to solve the equations of motion, the process is somewhat similar to doing iteration. Through the 4^{th}-order Runge Kutta method, the body velocities are solved four times for each time, t. This, along with a small Δt, should only contain a small error in the body velocities and displacements found. Body B's velocity is used to solve for the drag force.

3.5 Power Performance

The time series of the power output for the single-body and double-body cases are

$$P(t) = C_{DD}(\dot{z}(t))^2\beta \tag{3.47}$$

and

$$P(t) = C_{DD}(\dot{z_{rel}}(t))^2\beta, \tag{3.48}$$

where $P(t)$ is the time series of the power output and β is the gearing ratio. The gearing ratio is necessary to correlate the velocity of the body to the velocity the generator is rotating at. In this work, $\beta = 13$. The above equations are equivalent to

$$Power = Force * Velocity. \tag{3.49}$$

Because of conditions set on C_{DD} (see Section 3.3.4), power can only be generated when $\dot{z}(t) > 0$ or $\dot{z}_{rel}(t) > 0$ and $z_{rel}(t) > 0$.

CHAPTER 4

RESULTS AND DISCUSSION

4.1 Experimental Results

MATLAB was used to process the experimental outputs in Table 4.1. The single-body and double-body experimental data processing is the same.

Sensor Equipment	Output
Nortek Aquadopp	Depth (m)
Eagletree power logger	Voltage (mV)
Celesco RT8510 rotary sensor	Voltage(mV)

Table 4.1. Raw Data

To change the rotary sensor data to linear distance traveled, the mV is converted to degrees by use of the manufacturer's conversion ratio (0.13889 mV/degree). The length of the arc formula is used to convert degrees to linear distance. Because of how the equipment is connected, a gearing system was made where the displacement the rotary sensor records is 1/10th of the actual displacement the WEC system travels. Therefore, the displacement of the WEC is

$$L = \frac{n}{360} 2\pi r_{rs} \gamma$$

where n is the degrees rotated and γ is

$$\gamma = \frac{r_{spool}}{r_{rs}}$$
$$\gamma = \frac{3.17cm}{.317cm} = 10.$$

r_{spool} is the spool radius, and r_{rs} is the radius of the rotary sensor. The resulting displacement measurements are normalized to the first displacement of the ocean experiment. This sets initial displacement of the WEC system to be zero and the following data to be relative to the starting conditions. Similarly, the depth measurements were normalized by the depth of the top of the Aquadopp at the start of the first ocean experiment (17.43 m). It should be noted that the Aquadopp was on a frame that elevated the Aquadopp about 1 m off the sea floor.

The Eagletree power logger recorded the voltage across a 50Ω resistor. The instantaneous power generated is calculated by

$$P = V^2/R_L,$$

where V is the measured voltage across the resistor and R_L is the load resistor value.

From NOAA, the tidal data were given for the time and location of the experiments every 1 s. Since the data sets were at multiple sample rates, the WEC displacement, tidal, and Aquadopp data were interpolated to 10 Hz.

4.1.1 Single-body Case

Fig. 4.1 shows the sea surface elevation and the WEC system's heave displacement. Both are measured relative to the sea floor. The red line is the tidal change over time during the trial (NOAA, 2012).

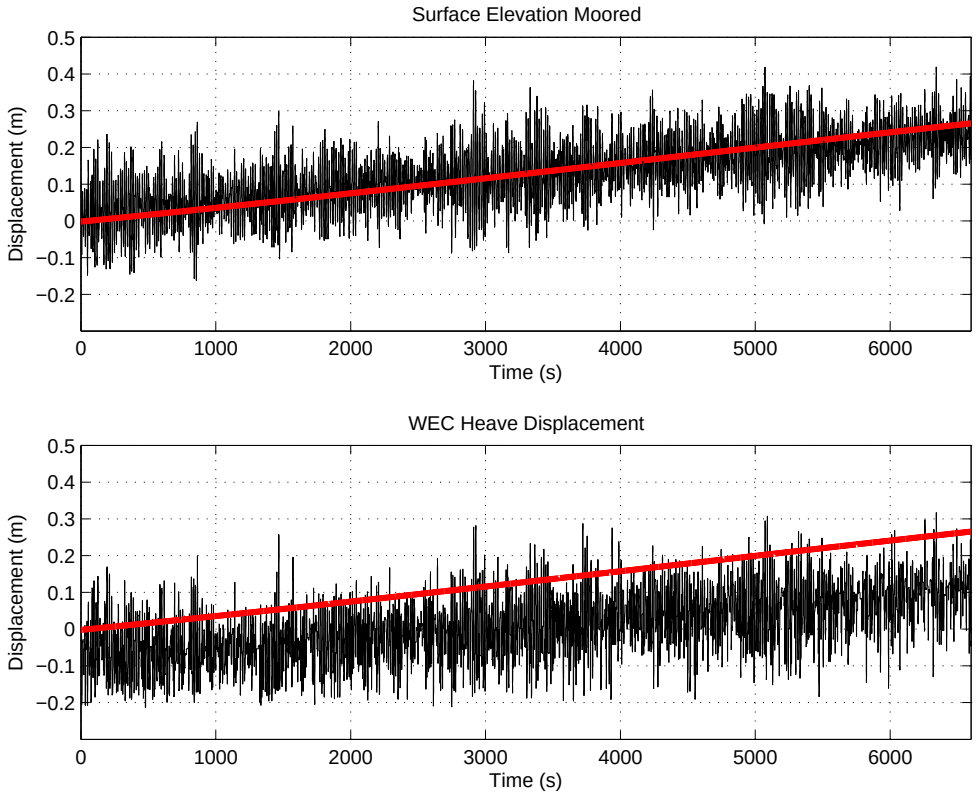

Figure 4.1. Surface elevation and WEC heave displacement with tide Lines

Sea surface elevation follows a positive upward slope because the distance between the sea floor and the still water level increased with the tide. This is also true for the surface elevation in the double-body case; therefore, the tidal components in both experiments were removed from the surface elevation data sets. The main effect the tide could cause is slamming in the WEC system if the mean water level increased by 60 cm, but because the test was not for a long duration, the change in tide level was not a main concern.

When the change in water elevation due to tide was overlaid with the WEC system's heave displacement, as in Fig. 4.1, it is noticeable that a drift force is acting

on the WEC system causing it to not exactly follow the tide line.

A vertical contribution of the horizontal drift is caused by the waves pushing the WEC system with each passing. A horizontal drift force causes a vertical displacement because of the finite length of the mooring line. This vertical displacement is recorded by the rotary sensor as it records the WEC system's motion along the mooring line.

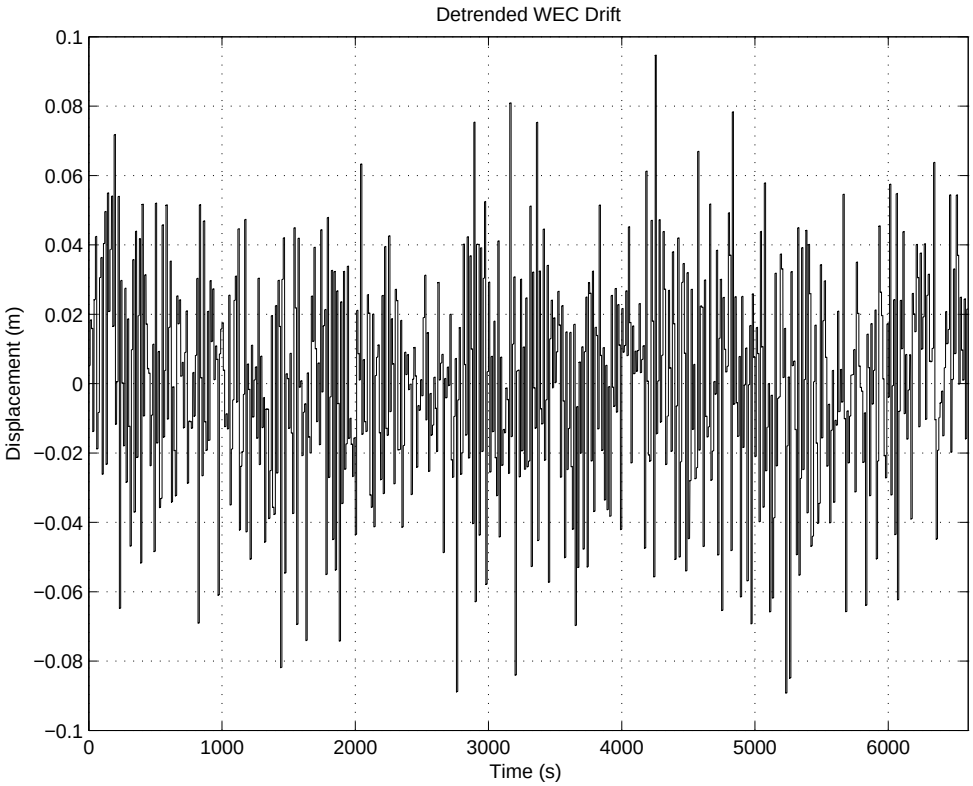

Figure 4.2. WEC vertical contribution of horizontal drift

The vertical component of horizontal drift, Drf, in Fig. 4.2 was found by Eq. (4.1). The drift was found for bins of N=100 data points of the WEC heave displacement,

WEC_D, and tide, Td, then removed. The drift for every 10 s is shown in Fig. 4.2.

$$\begin{aligned} \mathrm{Drf} &= \frac{\sum_1^N \mathrm{WEC}_D - Td}{N} \\ \mathrm{DWEC}_D &= \mathrm{WEC}_D - Td - \mathrm{Drf}. \end{aligned} \tag{4.1}$$

The detrended surface elevation and WEC system's heave displacement,$DWEC_D$, can be seen in Fig. 4.3

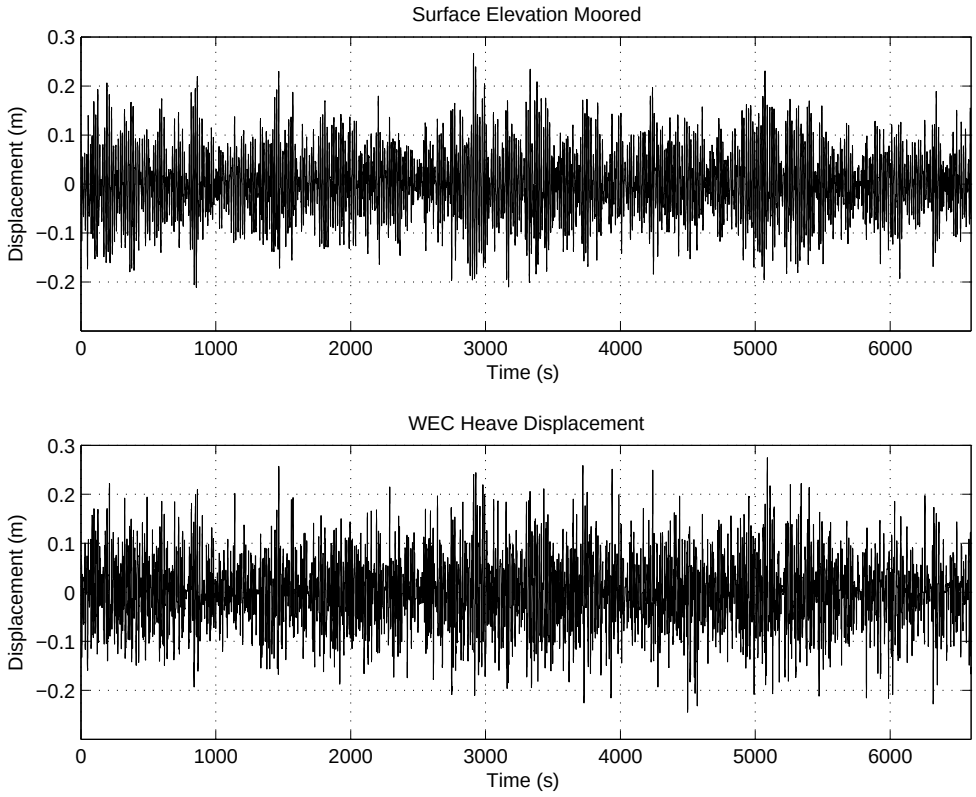

Figure 4.3. Detrended surface elevation and WEC heave displacement

From these time histories the significant wave height, H_s, can be found for the sea

surface and a significant heave displacement, Z_s, of the WEC system by

$$H_s = 4\sigma_{st} \tag{4.2}$$

$$Z_s = 4\sigma_{st} \tag{4.3}$$

where σ_{st} is the standard deviation of the respective time series.

Time History	Significant Values (m)
Sea Surface	0.2743
WEC system heave displacement	0.2745

Table 4.2. Significant values of ocean experiments

In Fig. 4.4, corresponding peaks are seen in the surface elevation, WEC system heave displacement, and power output. The power reaches a peak on the positive slope of the WEC system's heave displacement because power is only generated when the WEC system has a positive velocity. In other words, the WEC system only converts energy when heaving upward along the wave crest.

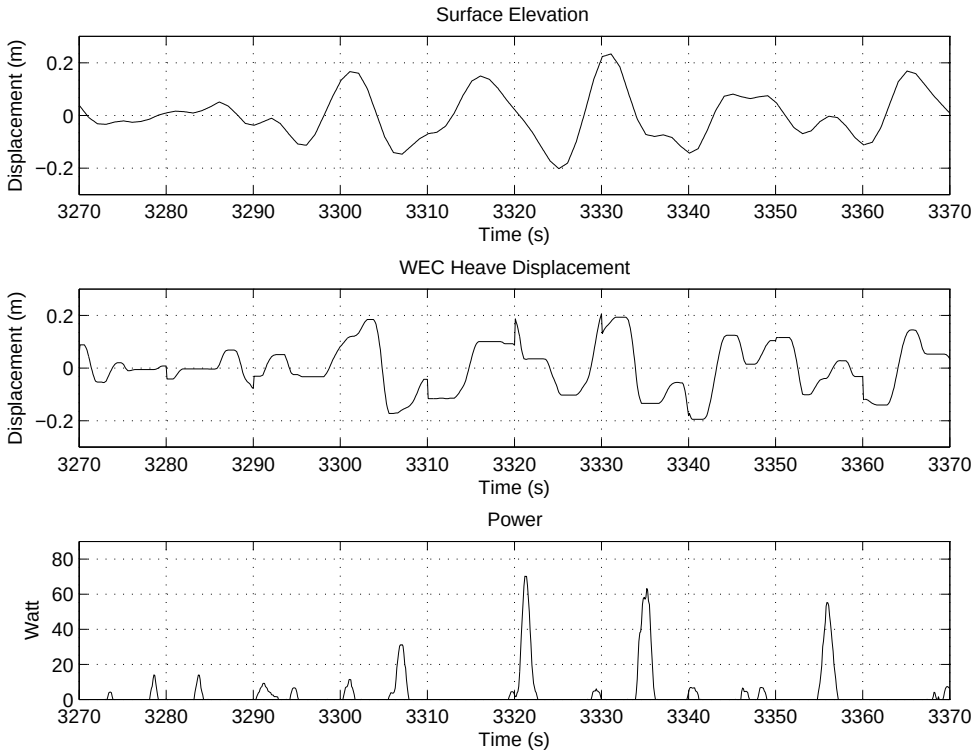

Figure 4.4. Section of the surface elevation, WEC heave displacement, and power

The maximum peak power output was 87 W and the average peak output over the experiment was 10.2 W, as shown by the red and blue lines, respectively, in Fig. 4.5.

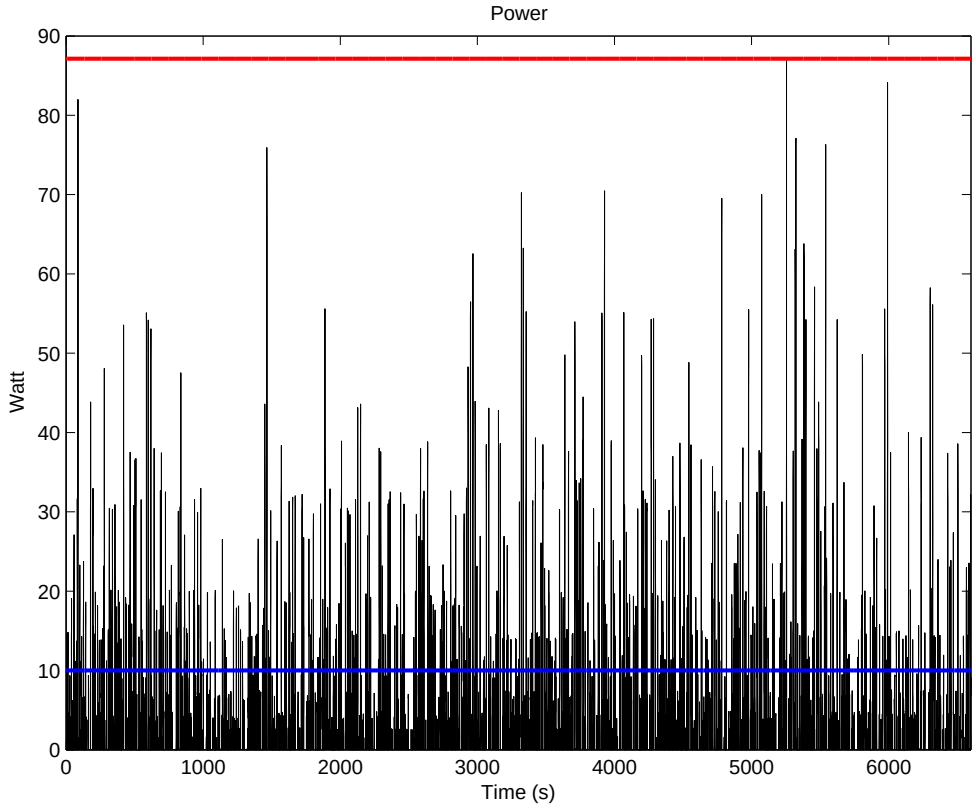

Figure 4.5. Power output

The mean RPM values were calculated to predict the power output for the WEC system connected to different electrical loads. The generator's average RPM was calculated from the rotary sensor's angular displacements by Eq. (4.4);

$$\begin{aligned} Rev &= \frac{n}{360}, \\ IRPM &= \frac{Rev}{dt} * 60, \\ RPM &= \beta * IRPM = 13 * IRPM \end{aligned} \tag{4.4}$$

where n is the degrees measured by rotary sensor, Rev is revolutions per time step, $IRPM$ is the instantaneous RPM, and β is the gearing ratio of the angular velocity of

the input gear to the angular velocity of the output gear. This is the same as β in Eq. (3.47). The RPM at the generator was 830 RPM. At 830 RPM, with a 24Ω load, the generator would have produced just over 200 W. With a load of 4Ω, a slightly higher resistance than for most 12 V Gel lead acid batteries, the WEC system's generator would have spiked around 350 W which could trickle charge a battery.

4.1.2 Double-body Case

Figure 4.6 shows the surface elevation with the tidal component removed, WEC system's heave displacement, and power output. For this case, no tidal components would be seen in the WEC system measurements. The spikes in the WEC system's heave displacement and power output do not match large surface elevation events.

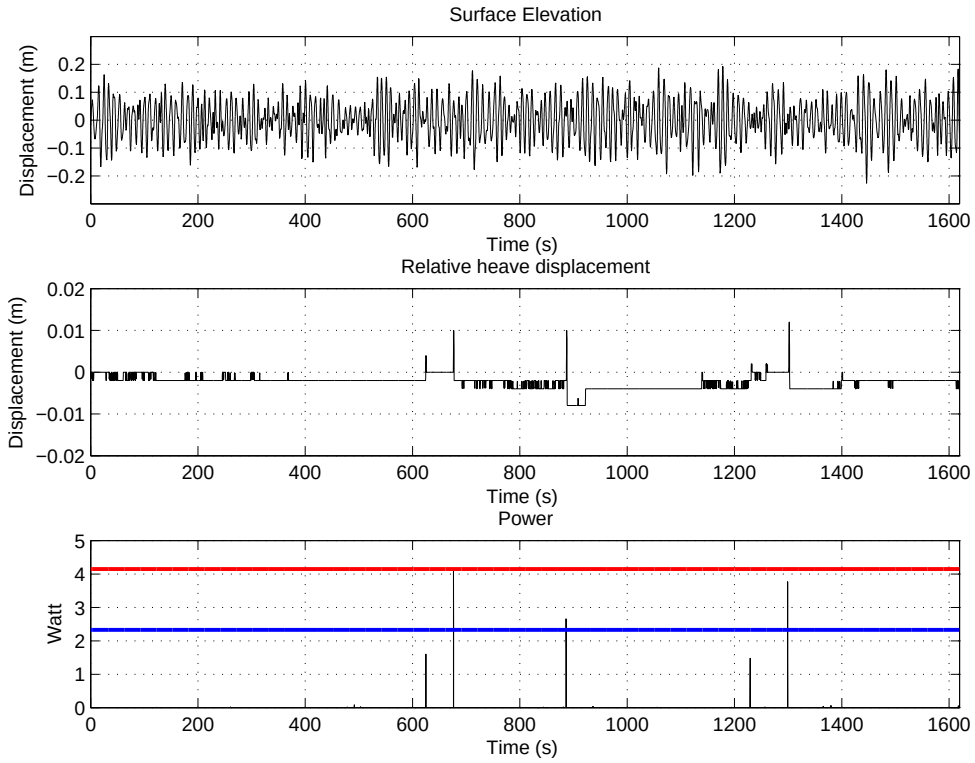

Figure 4.6. Surface elevation, WEC displacement, and power

The surface elevation in both cases had similar significant wave height and peak period values, 0.27 m and 15.5 s (found from the spectrum of sea surface elevation). However, only a slight WEC system displacement, less than 2 cm, was measured. This indicated that the drogue could not create enough anchoring resistance to enable the WEC system to capture wave energy.

The generator spun with an average of 16.4 RPM and a maximum of 232 RPM. At 232 RPM, with a 24Ω load, the generator would produce about 20 W. A load of 4Ω would produce about 50 W.

4.1.3 Filtered Data

Because of the results observed in the double-body case, only the single-body case measurements will be discussed further. The raw spectra of the surface elevation and WEC system's heave displacement are shown in Fig. 4.7.

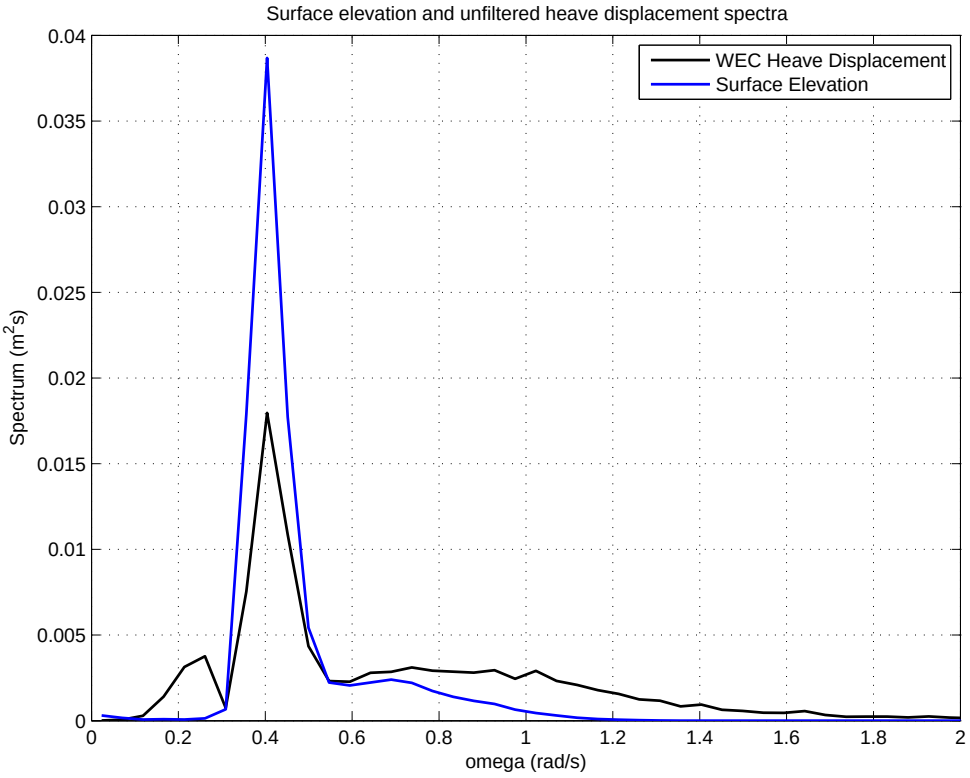

Figure 4.7. Unfiltered surface elevation and WEC heave displacement spectra

The larger WEC heave displacement spectrum at $\sigma < 0.3$ rad/s and $\sigma > 0.55$ rad/s should not happen, but we believe this was caused by the "clipping" seen in Figures 4.4 and 4.8.

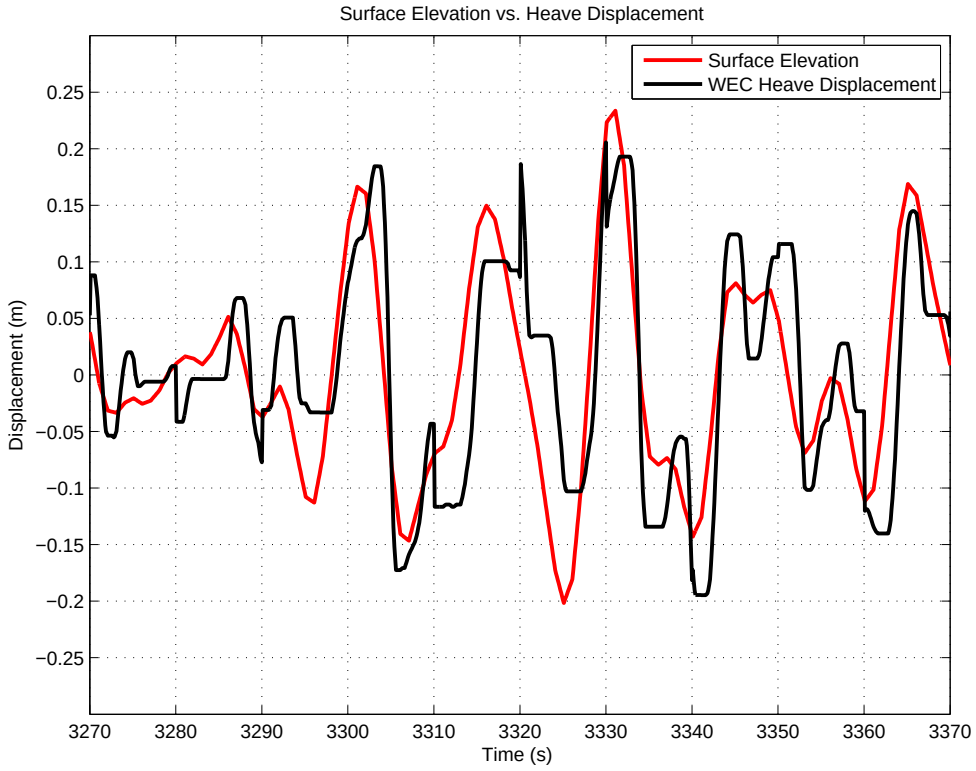

Figure 4.8. Detrended surface elevation and WEC heave displacement section

Figure 4.8 shows plateaus, or "clipping", in the WEC system's heave displacement. This occurs because of slight delay in the spring retracting which causes the device to delay for a few seconds. This "clipping" could be smoothed with digital filtering, but results in a lower standard deviation and Z_s. The H_s of the surface elevation and Z_s are found for the spectra by

$$H_s = 4\sqrt{\int_0^\infty S_{se}(\sigma)d\sigma} \tag{4.5}$$

$$Z_s = 4\sqrt{\int_0^\infty S_{WEC}(\sigma)d\sigma} \tag{4.6}$$

and are 0.2751 m and 0.2759 m respectively. The spectrally derived H_s and Z_s are similar to the time series derived H_s and Z_s in Table 4.1.1.

A 4^{th}-order digital Butterworth filter (0.14Hz and 0.048Hz) can be used to create a band-pass filter to eliminate the high and low frequency spikes from the WEC displacement signal seen in Fig. 4.7. In Fig. 4.9, the original WEC system's heave displacement is overlaid with the filtered heave displacement. The band-pass filter smoothed the clipped sections data but greatly reduced the Z_s of the WEC system to 0.19 m. Filtering should be used cautiously.

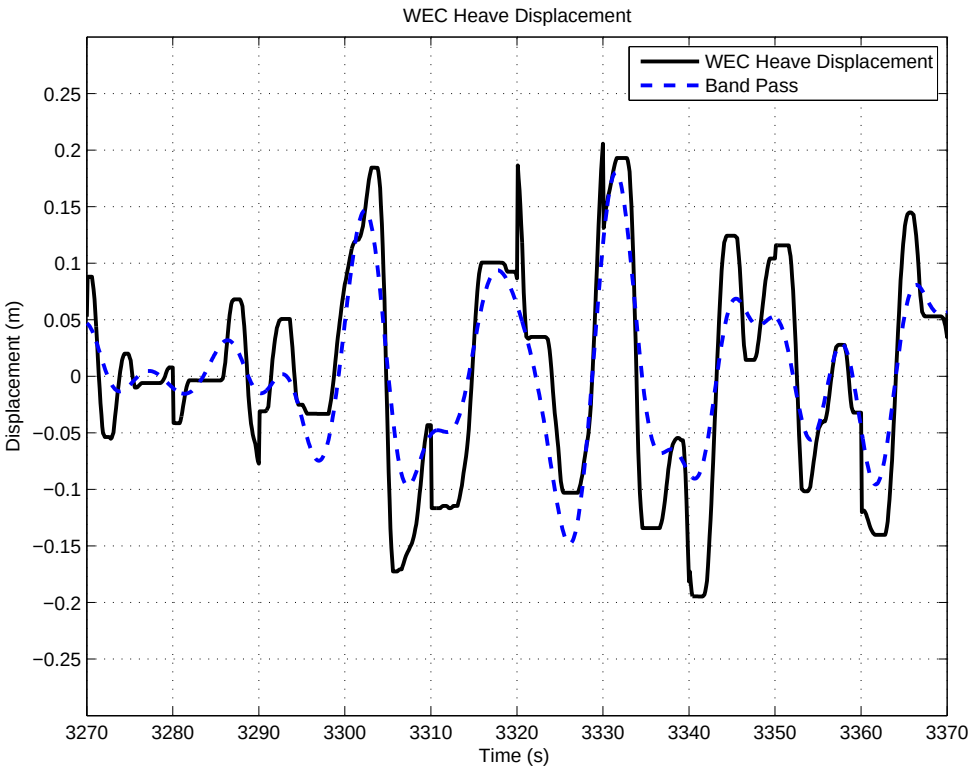

Figure 4.9. Section of bandpass filter and WEC Heave displacement

4.1.4 Spectrum and Response Amplitude Operator

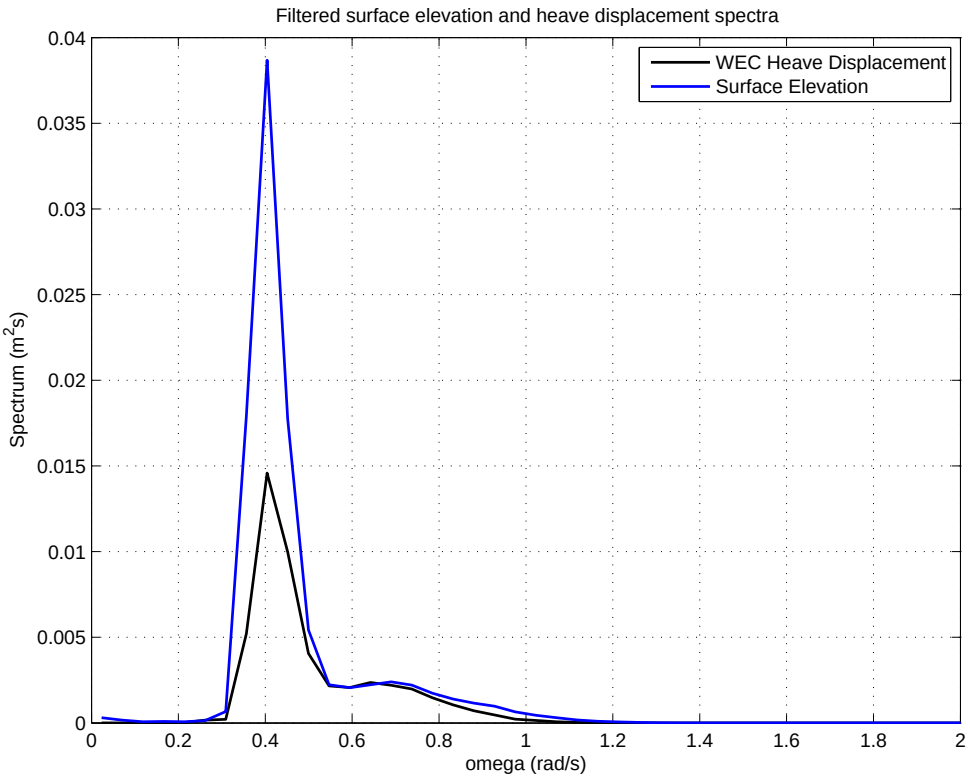

Figure 4.10. Wave and Heave Spectra

Figure 4.10 shows the spectra of the filtered WEC system's heave displacement and surface elevation data. The surface elevation's peak at 0.4 rad/s (peak period of 15.5 s) corresponds to the wave swell on the day of testing. The spectrum of WEC system's heave displacement gives a similar T_p of 15.5 s. This is because the WEC system rides the waves. The differences in the amplitudes of the two spectra is caused by wave damping and the PTO damping. The ratio between the two peaks, $S_z(\sigma)/S_{se}(\sigma)$ is the damping ratio, where $S_z(\sigma)$ is the spectrum of the heave displacement, $S_{se}(\sigma)$ is the spectrum of the surface elevation.

The heave response amplitude operator (RAO) in Fig. 4.11 is determined by

$$RAO = \sqrt{S_z(\sigma)/S_{se}(\sigma)} \tag{4.7}$$

The RAO defined from the filtered $S_z(\sigma)$ and $S_{se}(\sigma)$ shows little response at high frequencies and a unit response around 0.26 rad/s and 0.64 rad/s. Between 0.26 rad/s and 0.64 rad/s, a dip occurs, which corresponds to the damping ratio found in Fig. 4.10. When the WEC system converts wave energy, the RAO is less than 1.0; on the other hand, when the system was not excited enough to convert energy, it has a unit response to the incoming waves similar to a small floating cylinder. It is noted that this RAO can only be used for this case and cannot be used for other spectra since the system behaves nonlinearly due to power generation over only part of the wave cycle.

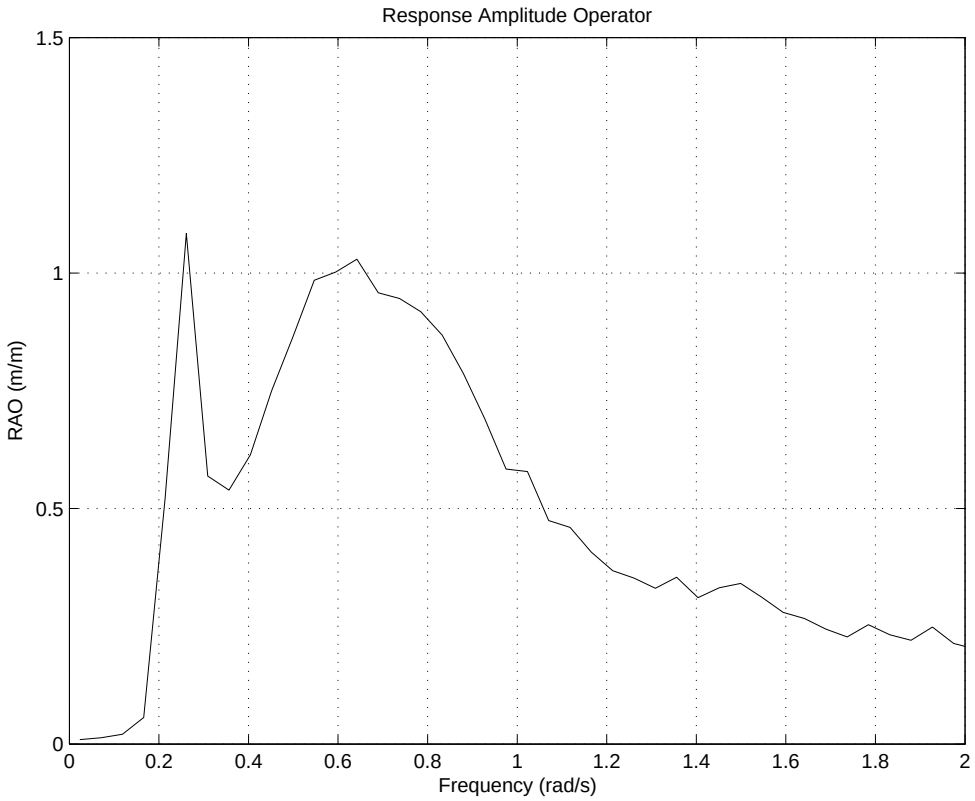

Figure 4.11. Heave RAO

4.2 Numerical Results

Once the numerical model is set for the body's wave exciting force transfer functions, added mass, damping, dimensions, body mass, and power take-off damping, the user defines the significant wave height, H_s, and peak period, T_p, at the desired site. This program can be used for a single wave spectrum or it could provide continuous output of power and displacements given a time series of H_s and T_p, such as seasonal or monthly data. The computational procedure of the numerical model can be outlined as seen in Fig. 4.12.

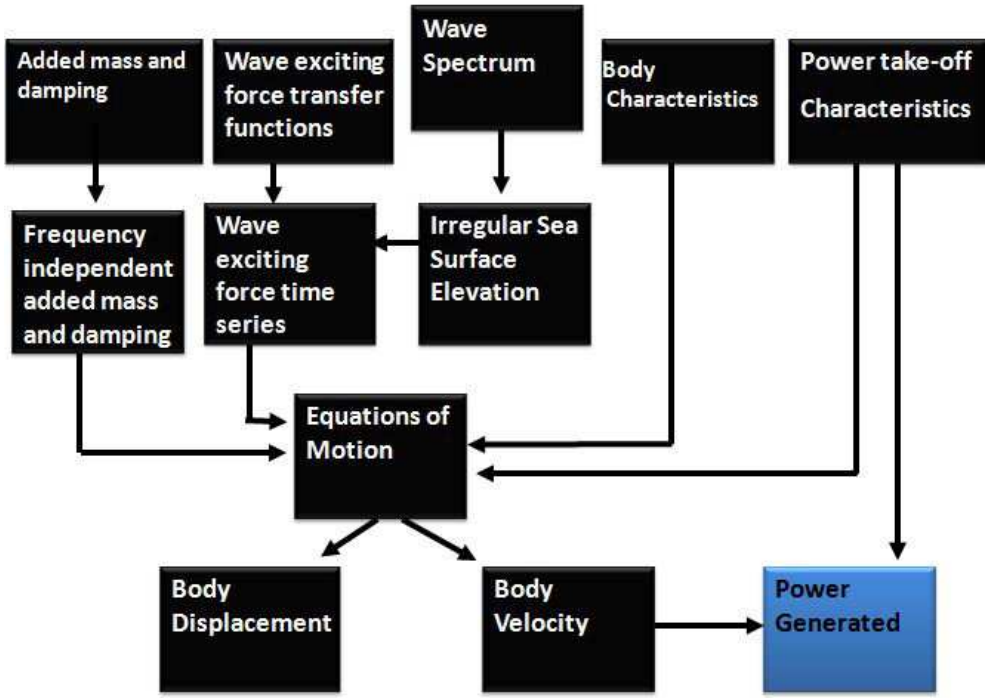

Figure 4.12. Program Flow Chart

For either case, the Bretschneider spectrum is calculated for the input H_s and T_p and for frequencies from 0.2rad/s to 2rad/s for a user define $d\omega$. For comparison with experiments, H_s=0.28 m, T_p = 15.5 s, $d\omega$ = 0.01 rad/s, $\alpha F_{constant}$ = 181 and $C_{DD} = 981Ns/m$ are used. Also, the motions and power output were calculated for C_{DD}=[2500,2000,1500,500] Ns/m values to assess the effect of C_{DD} on the results. The Bretschneider spectrum is shown in Fig. 4.13.

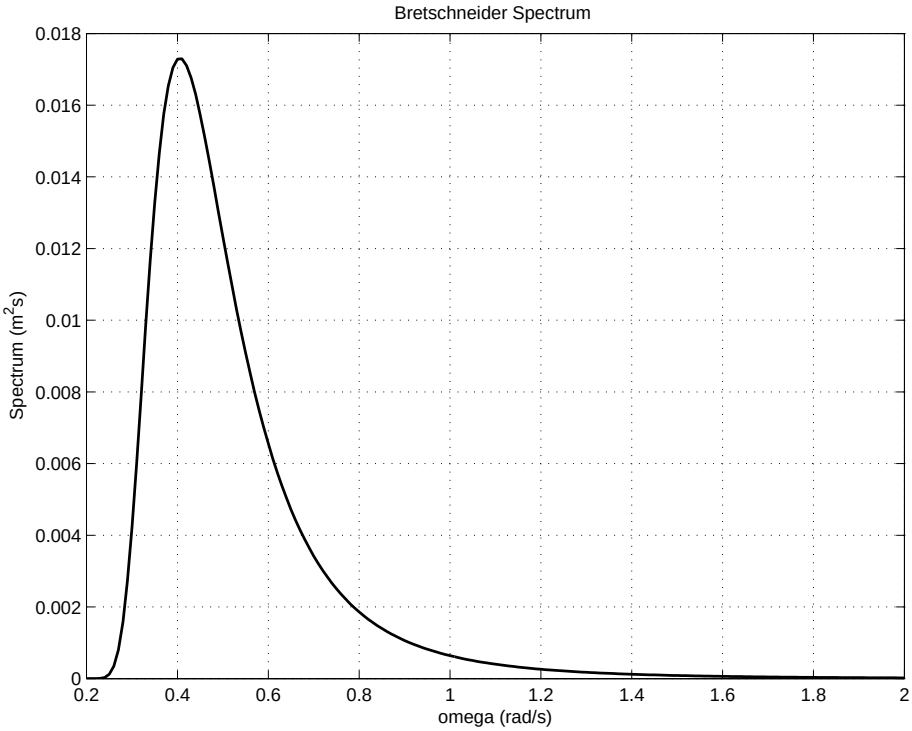

Figure 4.13. Bretschneider Spectrum, H_s=0.28 m and T_p=15.5 s

It should be noted that $d\omega$ should be sufficiently small to accurately represent the random seas with the correct variance and peak period. When going from a spectrum to sea surface elevation, the phase information is created by a random number generator. If the variance or peak period of the generated sea surface elevation are slightly off, $d\omega$ should be made smaller, or the sea surface elevation should be created multiple times with different phases, then averaged. The program checks the variance and peak period of the sea surface elevation by calculating the spectrum of the generated time series. The irregular sea surface elevation used for all numerical results in this paper is shown in Fig. 4.14. This sea surface elevation is used to solve both cases for all values of C_{DD}. It allows for a time comparison between the motions

and power output at any time t. The maximum, average, and location of the motions and power peaks will change with a different selection of random phase used to create the random time series data. The RMS remains similar with different time series.

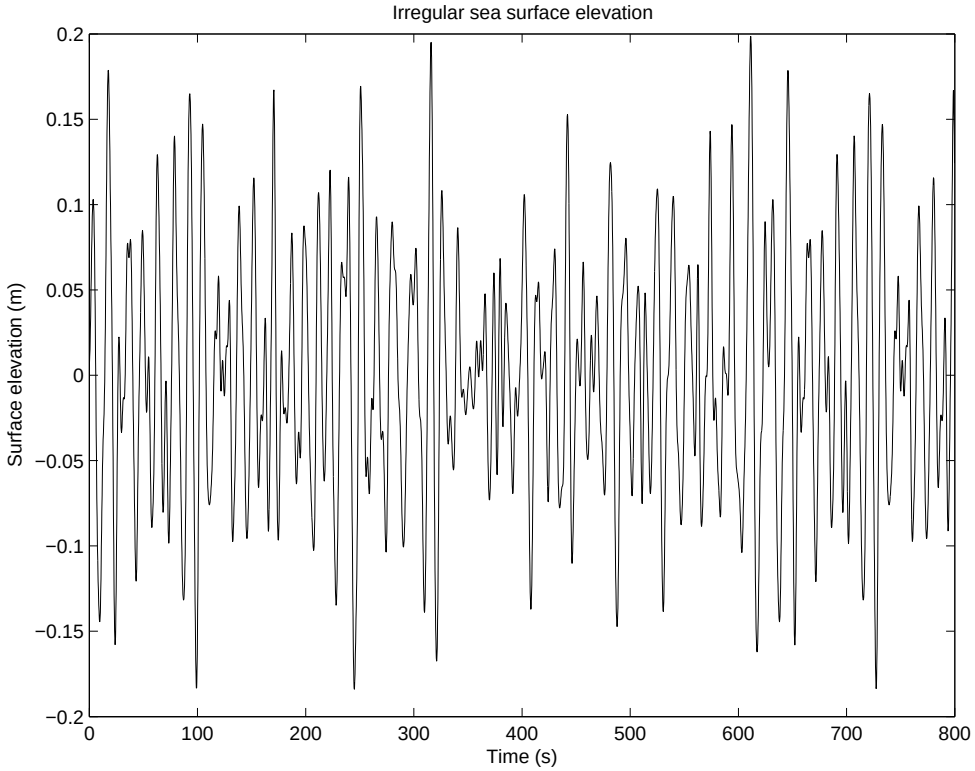

Figure 4.14. Irregular sea surface

The frequency domain force transfer functions and time series of sea surface elevation create the time history of the Froude-Krylov forces and diffraction forces acting on the body(bodies) as described in Section 3.3.1. The frequency dependent added mass and damping of the body (bodies) are used to solve for the frequency independent added mass and damping Kernel as described in Section 3.3.2. With all the forces and initial conditions known, the 4^{th}- order Runge Kutta method is used to solve the coupled 1^{st}-order ODEs for the equations of motion as described in Section

3.4. From the results of the equations of motion, the power output is calculated and output.

4.2.1 Single-Body Case

The input values for the single-body case are shown in Fig. 4.15-4.17. The damping and added mass are calculated for frequencies of 0.2 to 9.7 rad/s, as seen in Fig. 4.15.

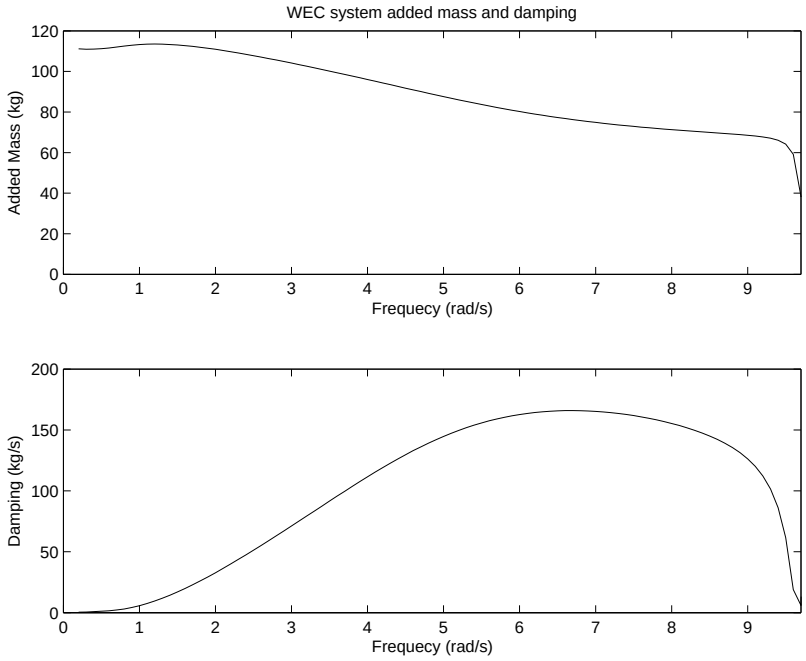

Figure 4.15. WEC system's added mass and damping

This range is used so the damping goes back down to zero, and the Kernel function converges to zero as seen in Fig. 4.18. The Froude-Krylov and the diffraction force transfer functions of the WEC system are shown in Fig. 4.16 and Fig. 4.17.

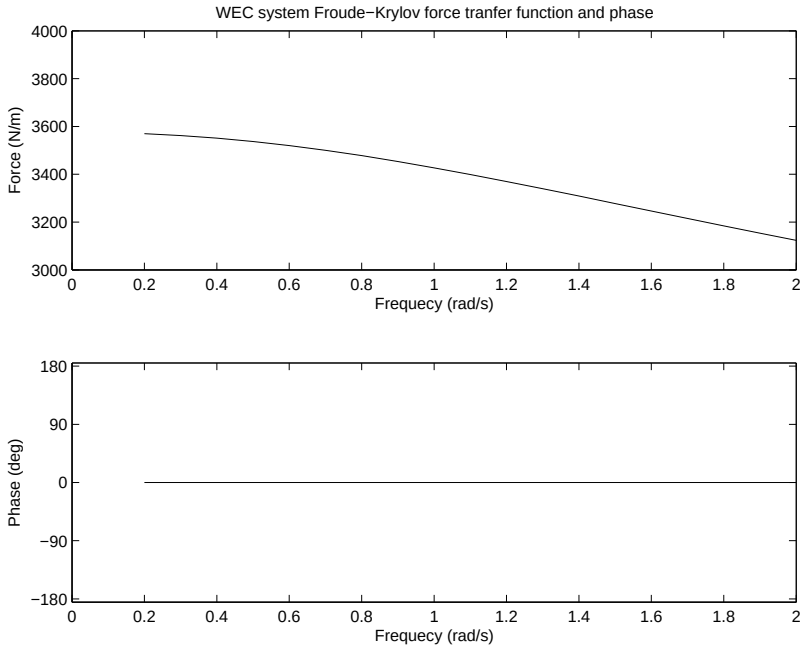

Figure 4.16. WEC system's Froude-Krylov force transfer function and phase

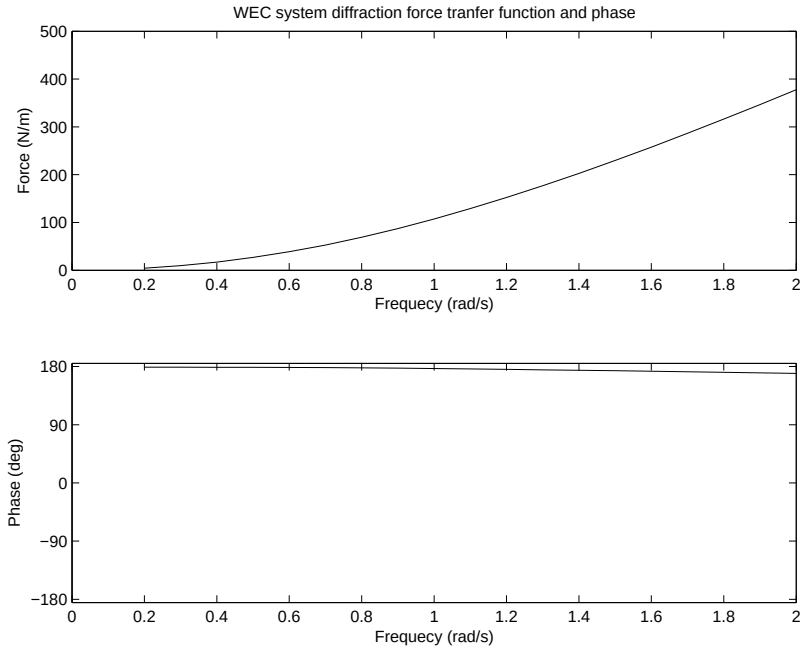

Figure 4.17. WEC system's diffraction force transfer function and phase

The resulting Kernel function, see Fig. 4.18, shows that $K(\tau)$, reaches near a constant

value with Filon's method at approximately $\tau = 30s$. The infinite-frequency added mass for the single-body case and Body A are taken as 78 kg.

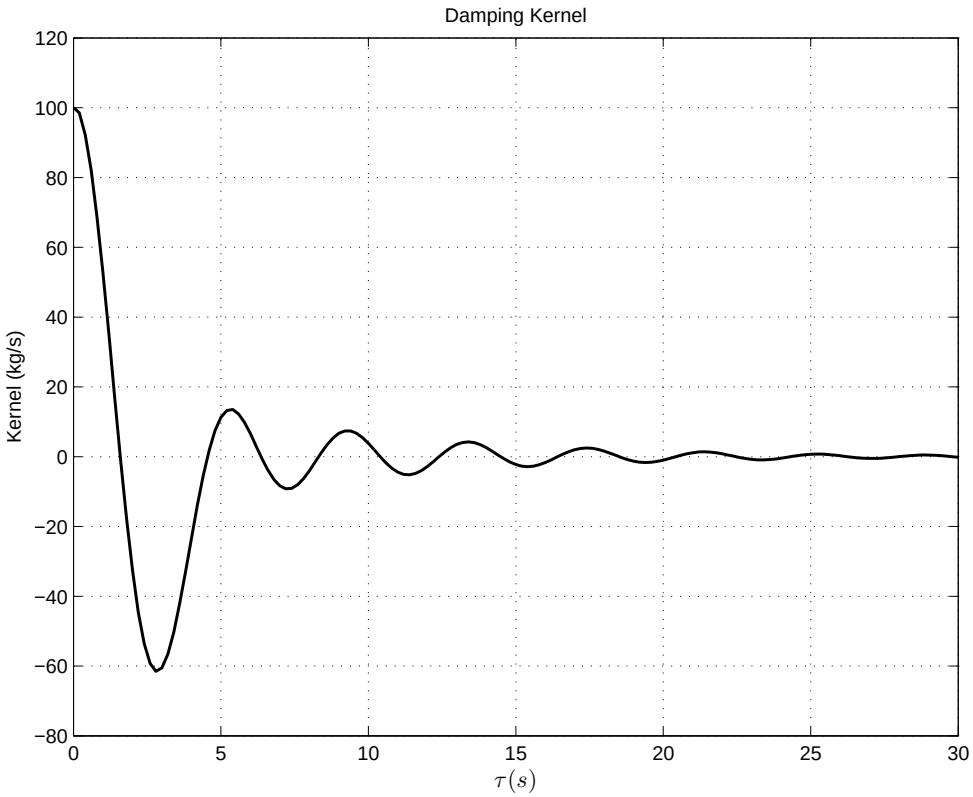

Figure 4.18. Kernel of the WEC system

Figure 4.19 shows the wave exciting forces and wave elevation as a function of time. It is noticeable that the Froude-Krylov force has the same shape as the wave elevation. This is because the phase of the Froude-Krylov forces is constant (as seen in Fig. 4.16) and the same as the surface elevation. The time series of the diffraction force is the third plot in Fig. 4.19. The wave exciting forces is the summation of the complex Froude-Krylov forces and the complex diffraction forces. The wave exciting force in Fig. 4.19 is similar to the time series of the Froude-Krylov force because the

diffraction forces are an order of magnitude smaller than the Froude-Krylov forces.

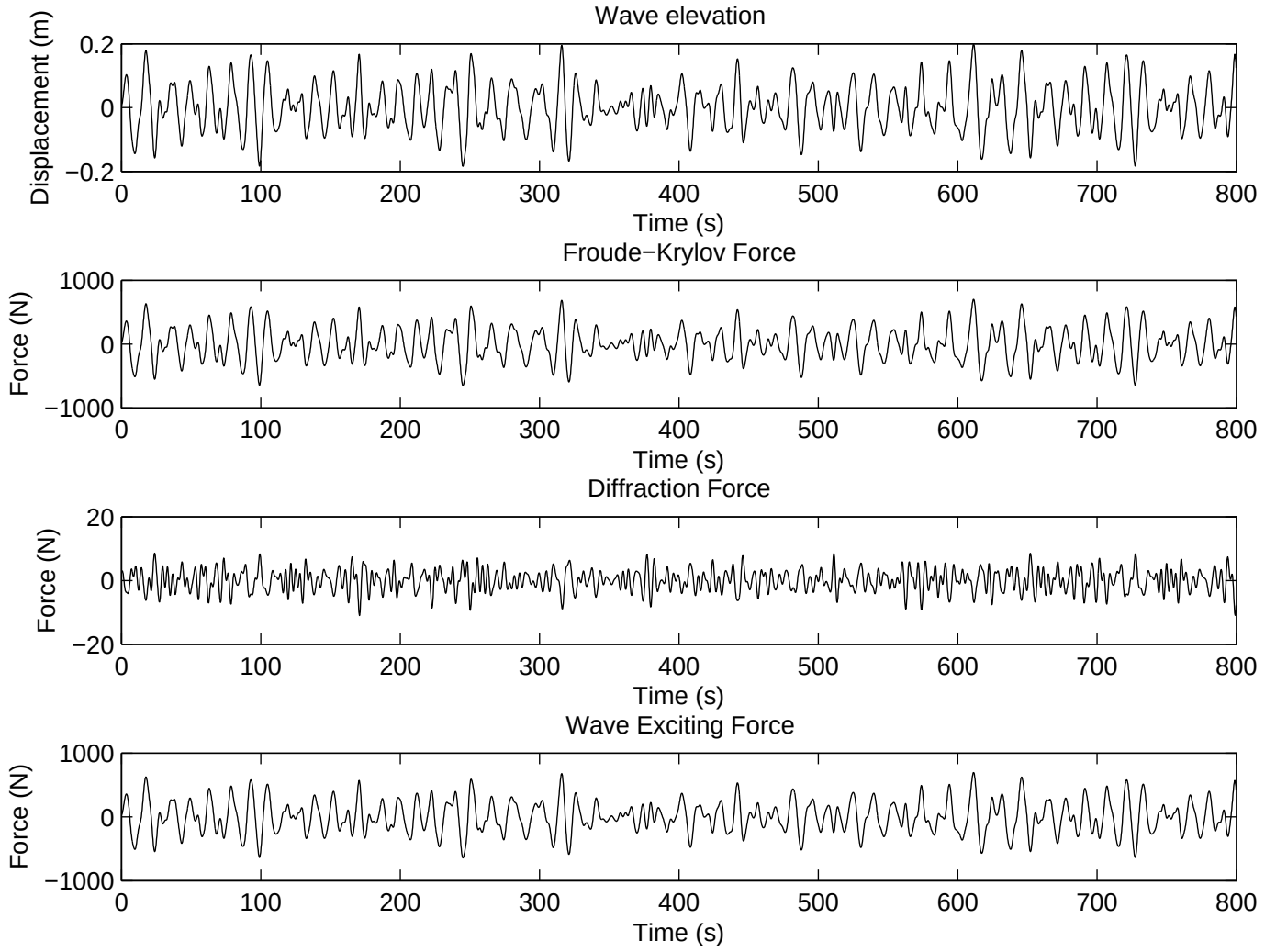

Figure 4.19. Time series forces acting on the WEC system.

Figure 4.20 shows the WEC system's heave displacement compared to the surface elevation. This shows that the WEC system closely follows the waves with slightly smaller amplitudes. This is similar to what is observed in the experimental data in Figures 4.4 and 4.8. The first 20 seconds of time series data should be ignored. It contains transient results from the arbitrary initial conditions of the body.

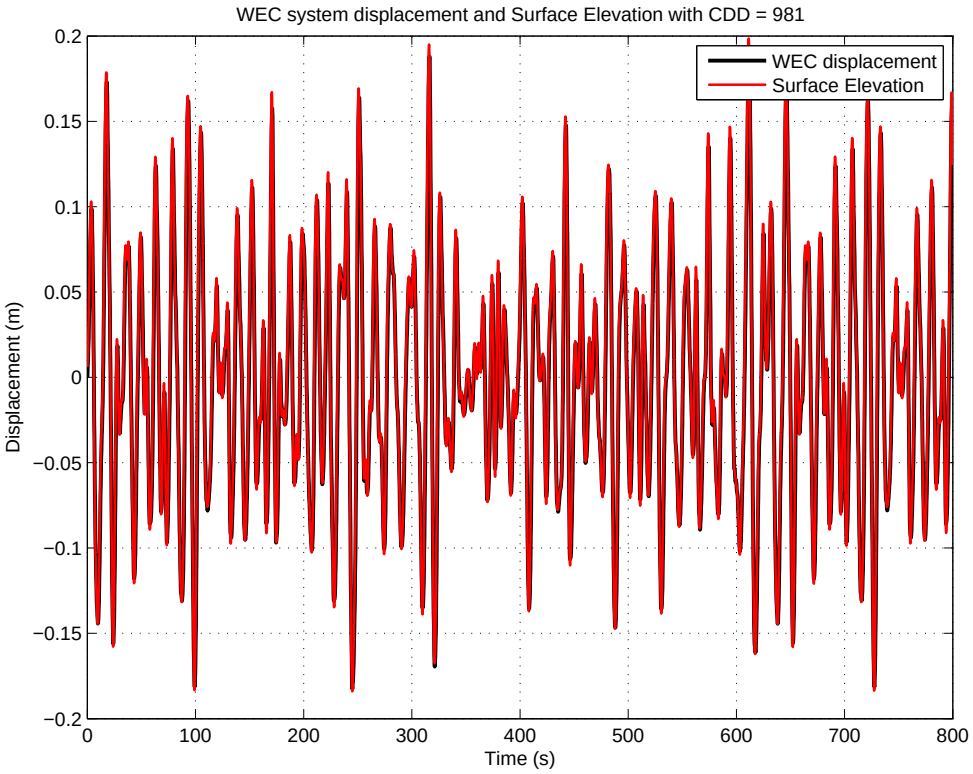

Figure 4.20. WEC system heave displacement versus surface elevation

The resulting spectra and RAO are shown in Fig. 4.21 and Fig. 4.22, respectively.

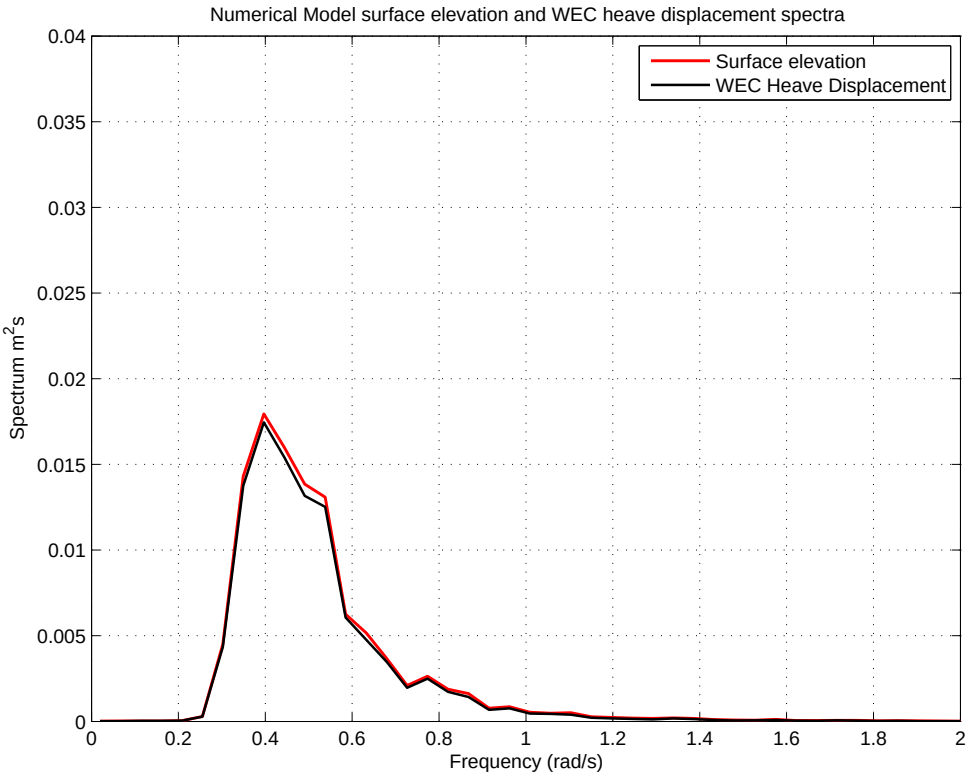

Figure 4.21. WEC system heave displacement and surface elevation spectra

The spectra show a difference in amplitudes at $\sigma = 0.4\ rad/s$ to $0.5\ rad/s$ where most of the energy is being extracted from the waves. Similar to the experimental data, Z_s=0.2752 m and $H_s = 0.28\ m$.

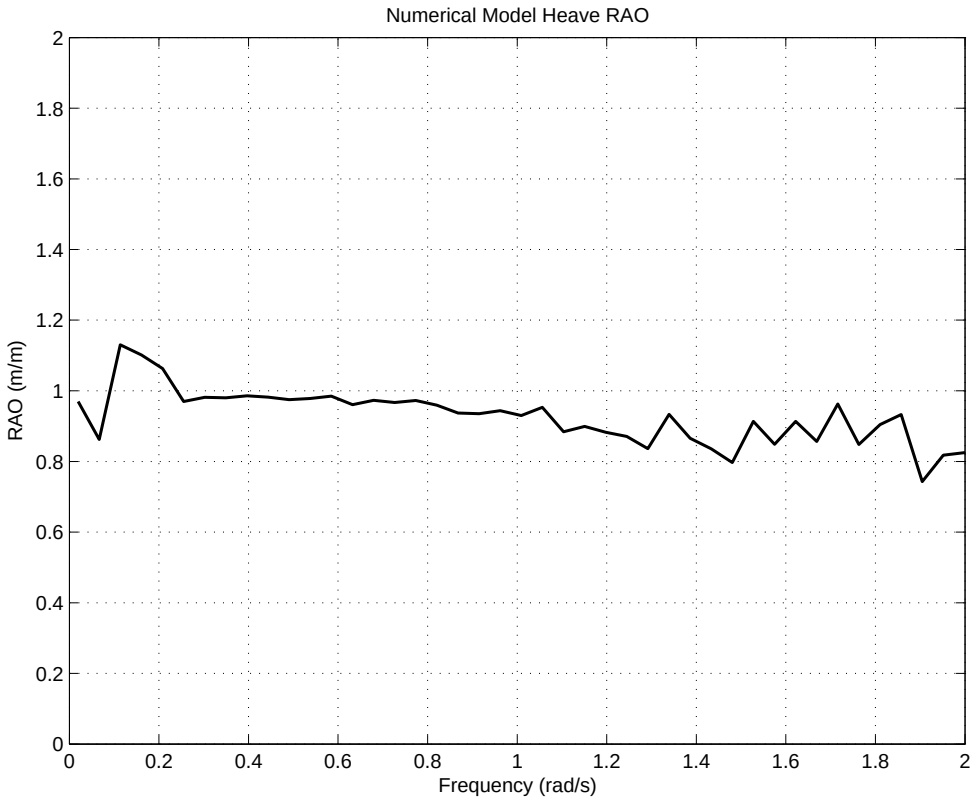

Figure 4.22. WEC system RAO

The RAO is around 1.0 for the entire frequency range. This is expected from observing the time series and spectra data (the WEC closely following the surface elevation). For this particular sea surface elevation, the results closely resemble a linear system. However, because the system is nonlinear, the RAO is only applicable to this spectrum. If the RAO is desired for another spectrum, the time series has to be recalculated and another RAO must be obtained. The resulting time series of power output is shown in Fig. 4.23.

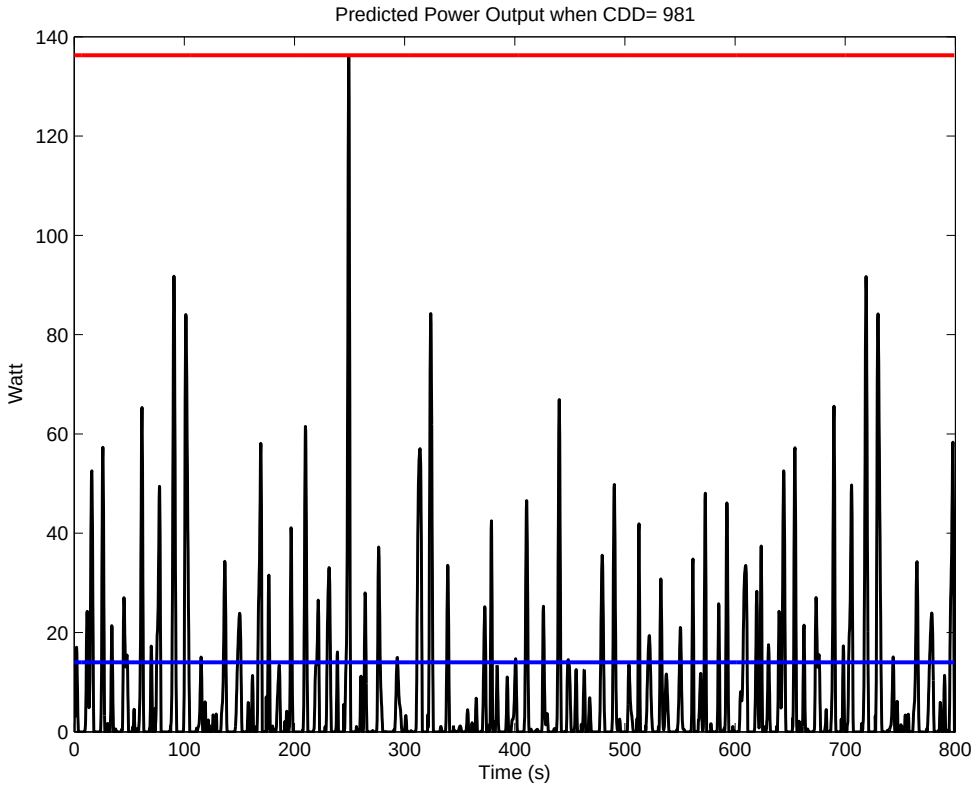

Figure 4.23. Time series of single-body power output

The maximum power output in Fig. 4.23 is around 140 W. This is just under double of the maximum peak for the ocean experiments, and is a result of the random phases that could produce this spike. The maximum peak power output and the average peak output over the time series are shown by the red and blue lines, respectively. The average peak output over the time series is 13.9 W, which is slightly higher than the experimental power output (10.2 W) in Fig. 4.5.

To double check the single-body program, C_{DD} was set to zero; therefore, no PTO was acting on the system and the buoy should act like a small floating cylinder. This linear system resulted in the buoy riding the wave, with the main variations caused

by the memory integral. The RAO of the WEC system with $C_{DD} = 0$ is 1 as seen in Fig. 4.24, and this concurs with the results for a freely floating cylinder.

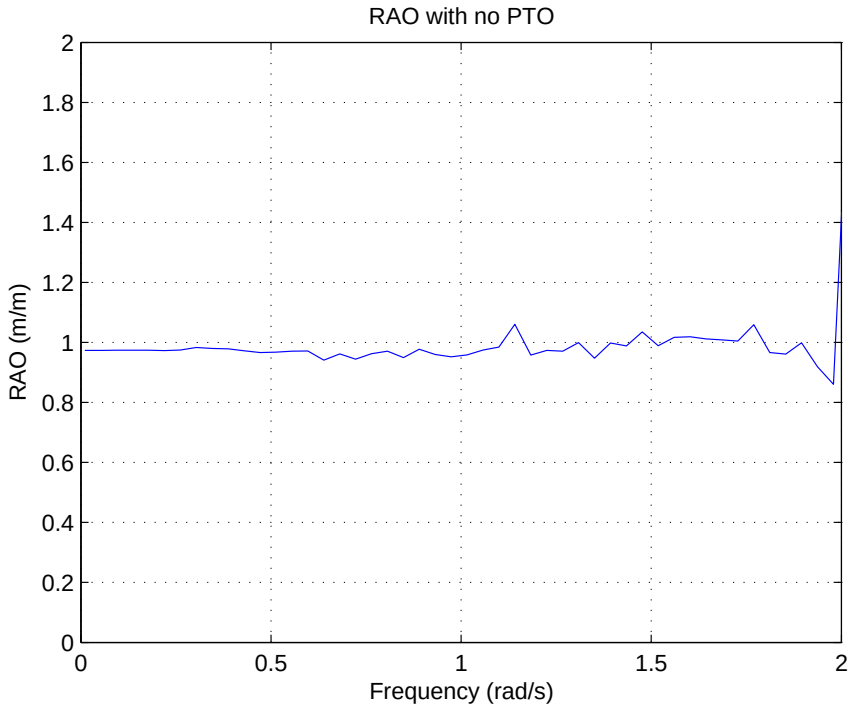

Figure 4.24. WEC system RAO with no PTO

Caution should be used when taking the spectrum of the WEC's heave displacement in that the WEC system is a nonlinear device which causes nonlinear motions.

4.2.1.1 Different Power Take-offs

Figure 4.25 shows that the larger the C_{DD} the greater the nonlinear effects on the body motion. A difference is seen in the leading edge of the waves for large C_{DD} values. The difference is cause by the C_{DD} restricting the body's motion when the

body has positive velocity. For smaller C_{DD} values, the body's motion is very close to sea surface elevation and the body acts like a linear system.

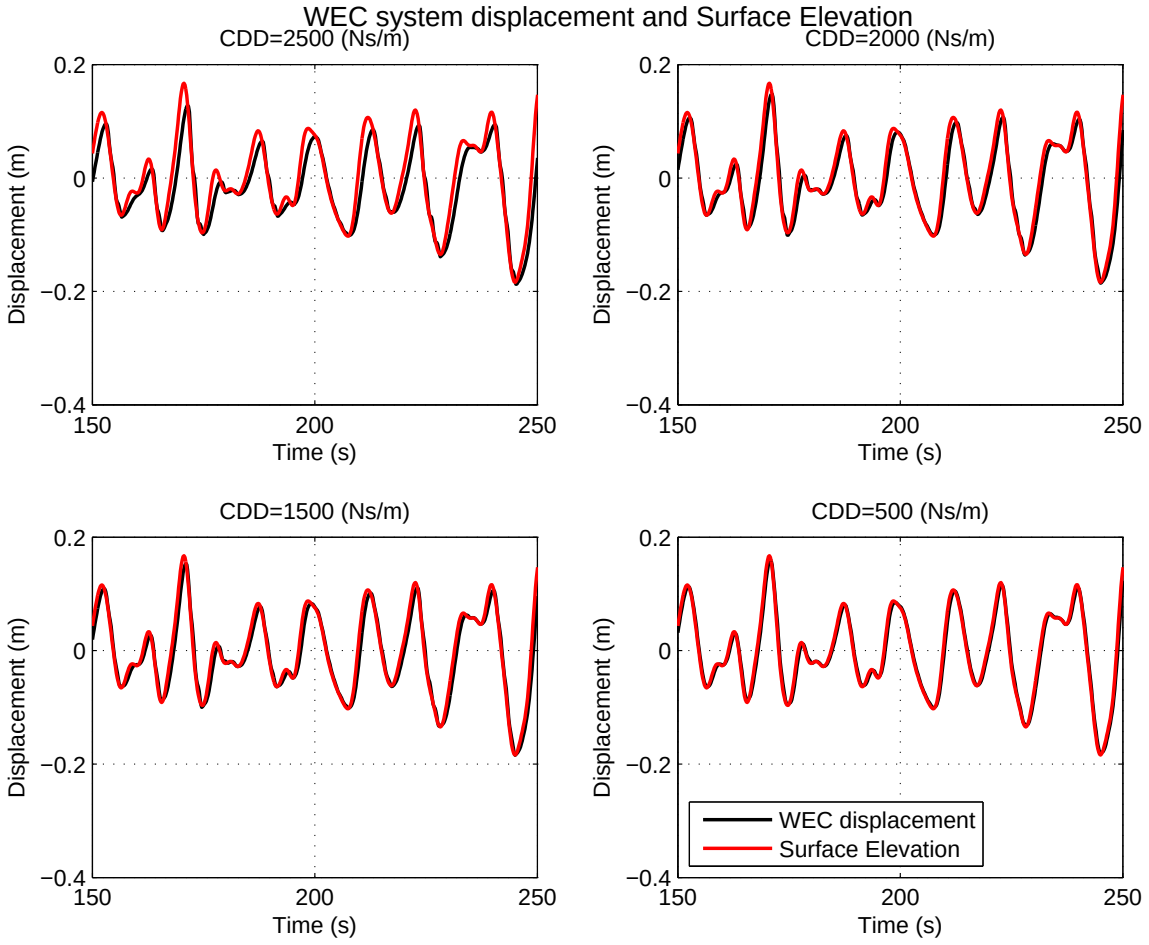

Figure 4.25. WEC system displacement for various C_{DD} values

Figure 4.26 shows that $C_{DD} = 2500Ns/m$ is not ideal for the WEC system. The body is overdamped, has a mostly negative velocity, and is thus unable to produce power. As C_{DD} decreases, the positive velocity increases. Therefore, for power generation, a trade off has to be made between the C_{DD} value and the velocity. A higher C_{DD} will generate more power but too high a C_{DD} will decrease the positive velocity

and thus decrease the power output.

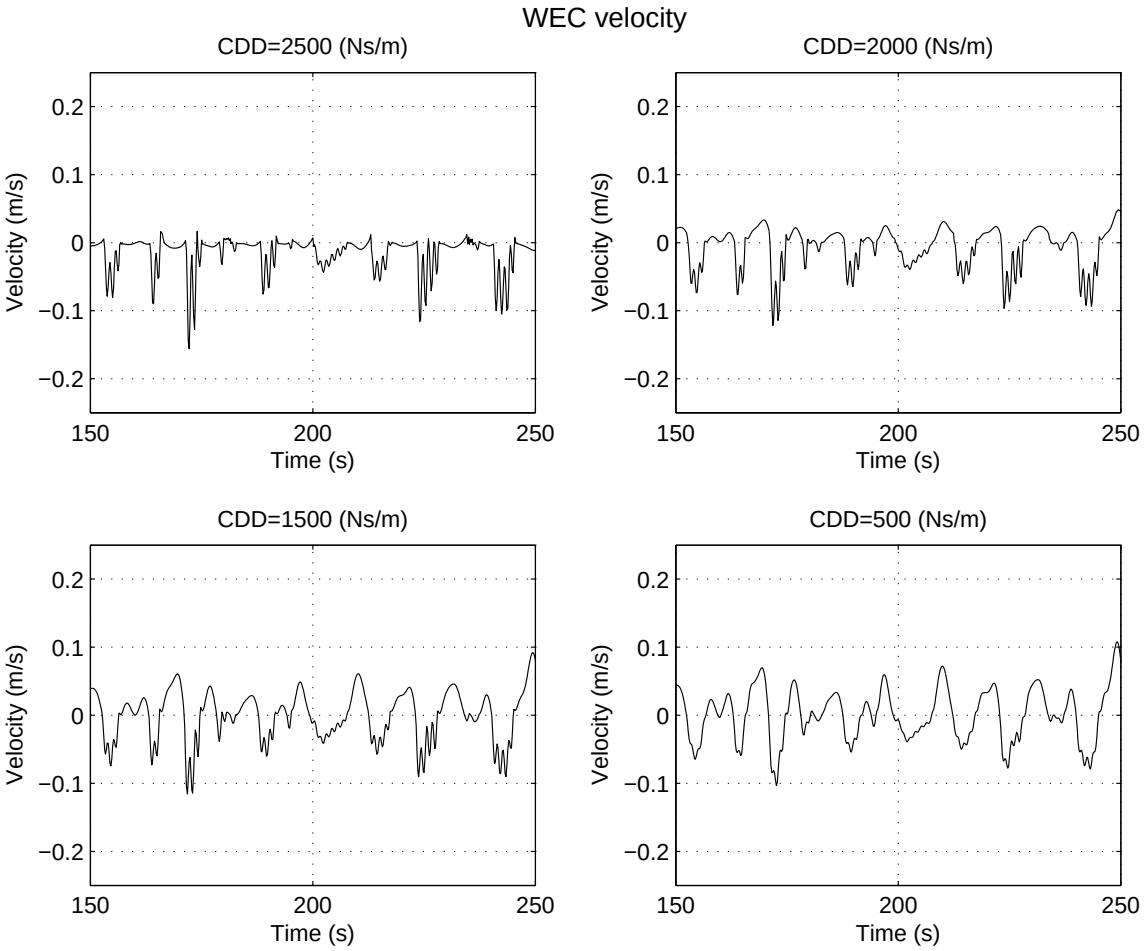

Figure 4.26. WEC system velocity for various C_{DD} values

The overdamping with $C_{DD} = 2500Ns/m$ is also seen in Fig. 4.27, as it has low power output and the least number of peaks. $C_{DD} = 500Ns/m$ creates a system that is underdamped as it produces the least power with a similar amount of peaks as $C_{DD} = 2000, 1500$. By studying the plots of $C_{DD} = 2000Ns/m$ and $C_{DD} = 1500Ns/m$, it seems that an optimum C_{DD} value is near $1500Ns/m$ for this case.

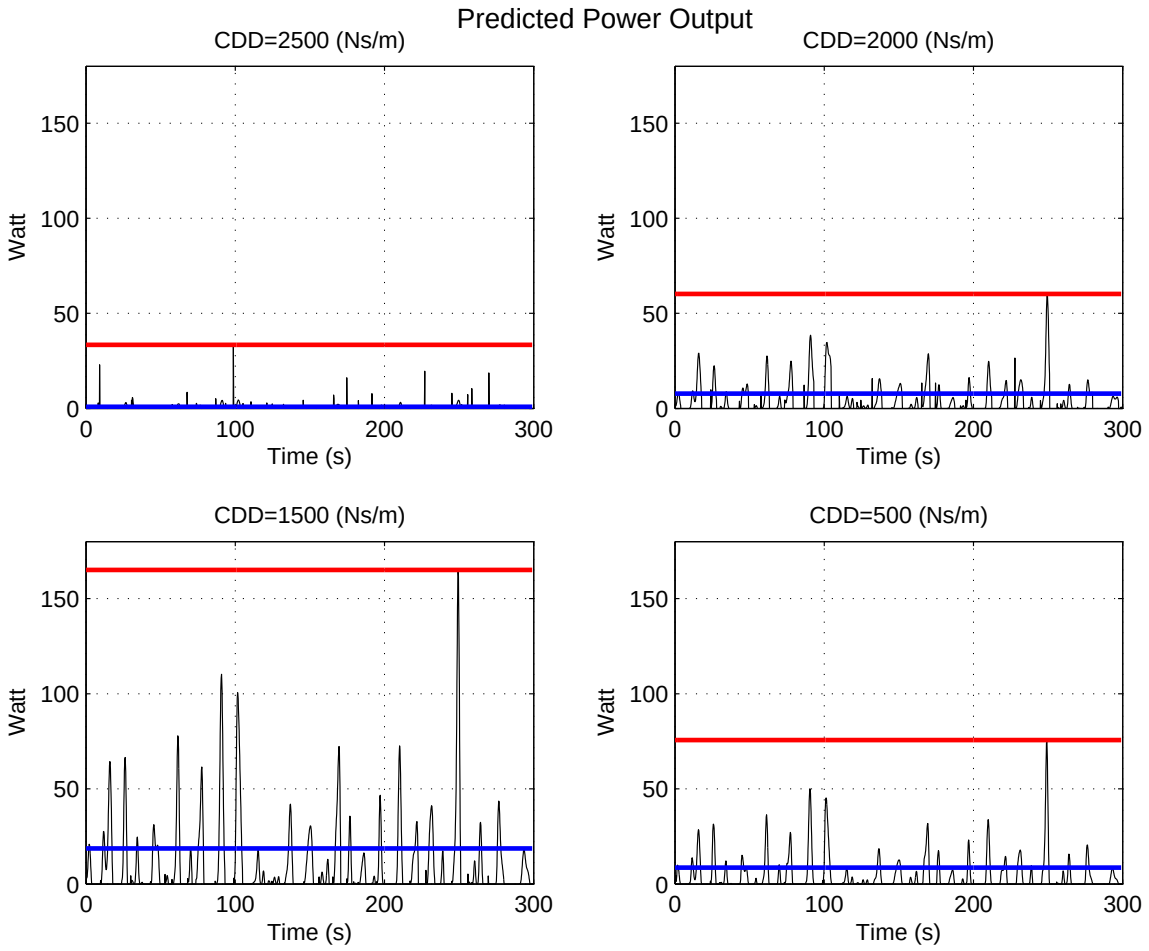

Figure 4.27. Power output for various C_{DD} values

For each case, the maximum peak power output and the average peak output are shown by the red and blue lines, respectively.

4.2.2 Double-Body Case

The single-body case inputs are shown in Fig. 4.15 to Fig. 4.17. The drogue inputs are shown in Fig. 4.28 to Fig. 4.30. As seen in Fig. 4.28, the damping is zero and the added mass is constant at 99 kg.

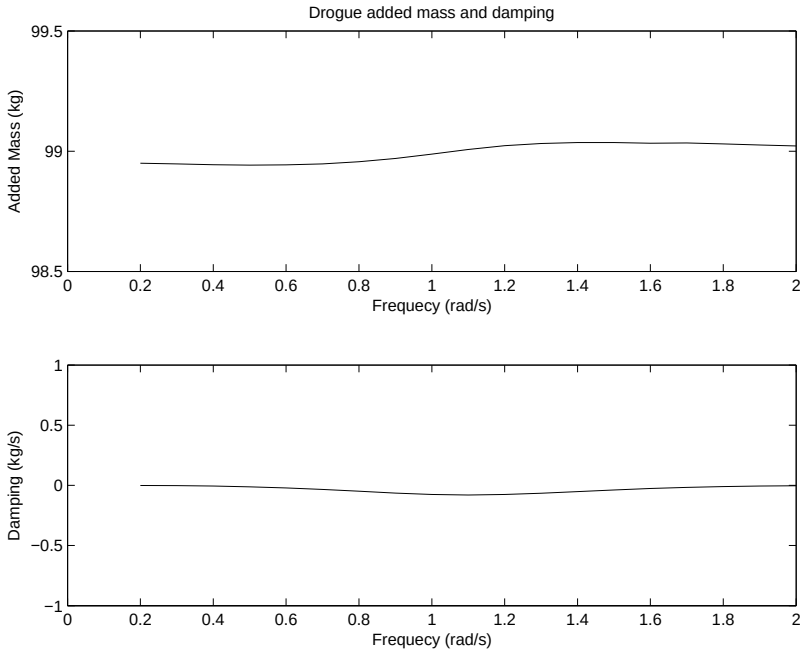

Figure 4.28. Drogue's added mass and damping

The Froude-Krylov force transfer function and the diffraction force transfer function have the same order of magnitude.

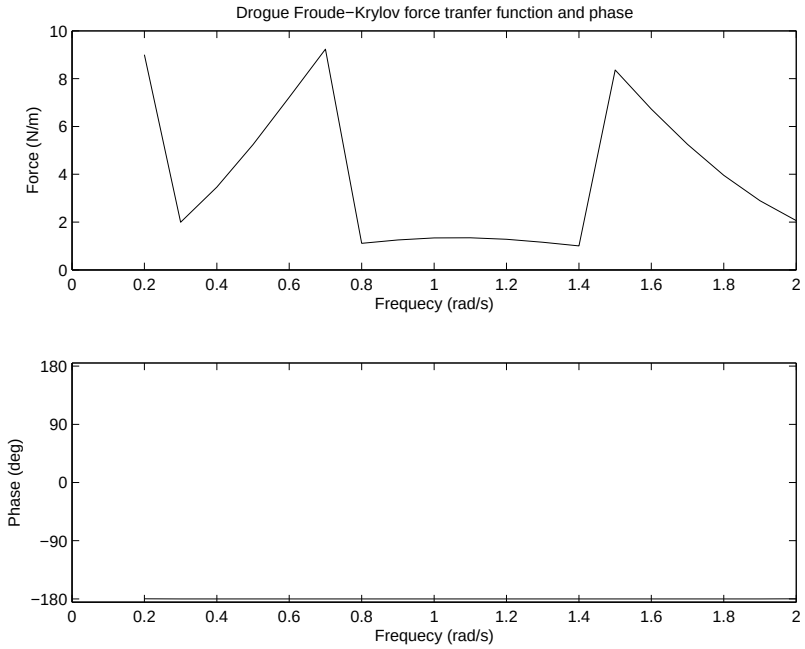

Figure 4.29. Drogue's Froude-Krylov force transfer function and phase

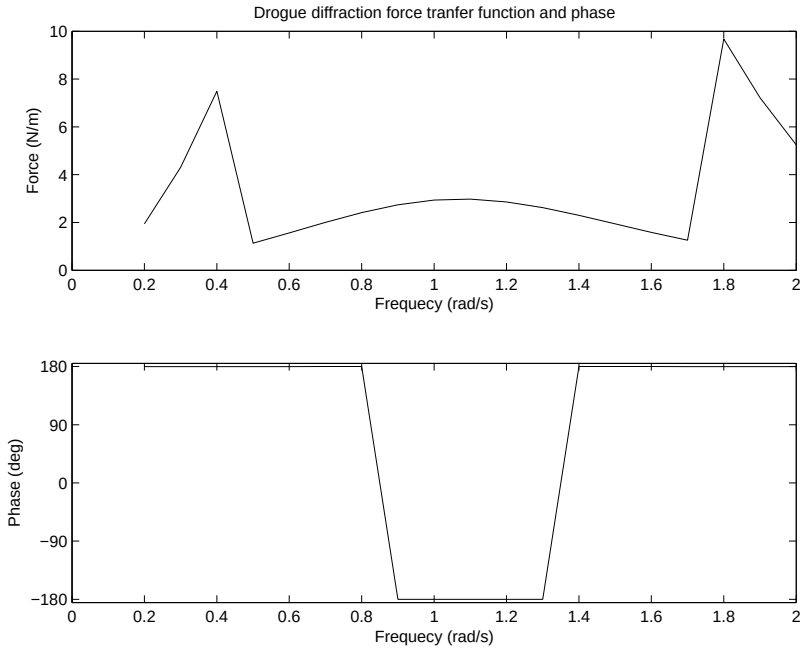

Figure 4.30. Drogue's diffraction force transfer function and phase

Figure 4.31 shows the wave exciting forces as a function of time. The wave exciting

forces in Fig. 4.31 are from the summation of the complex Froude-Krylov forces and the complex diffraction forces.

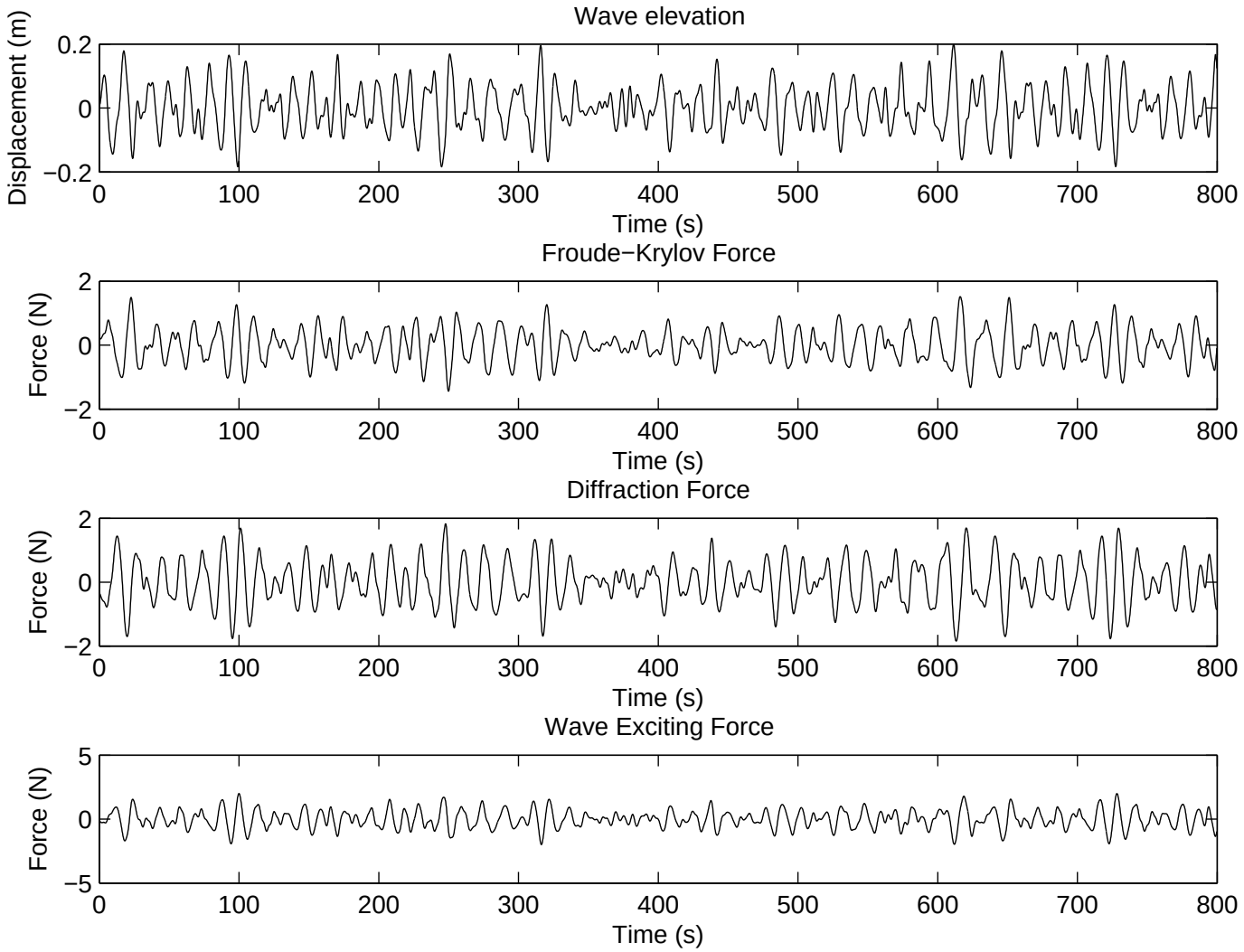

Figure 4.31. Time series forces acting on the drogue.

Figure 4.32 shows that Body A closely follows the waves with slightly smaller amplitudes, and Body B does not directly follow the sea surface elevation. Body B is jerked up at the crest of the wave by the PTO, and slowly sinks to its starting position.

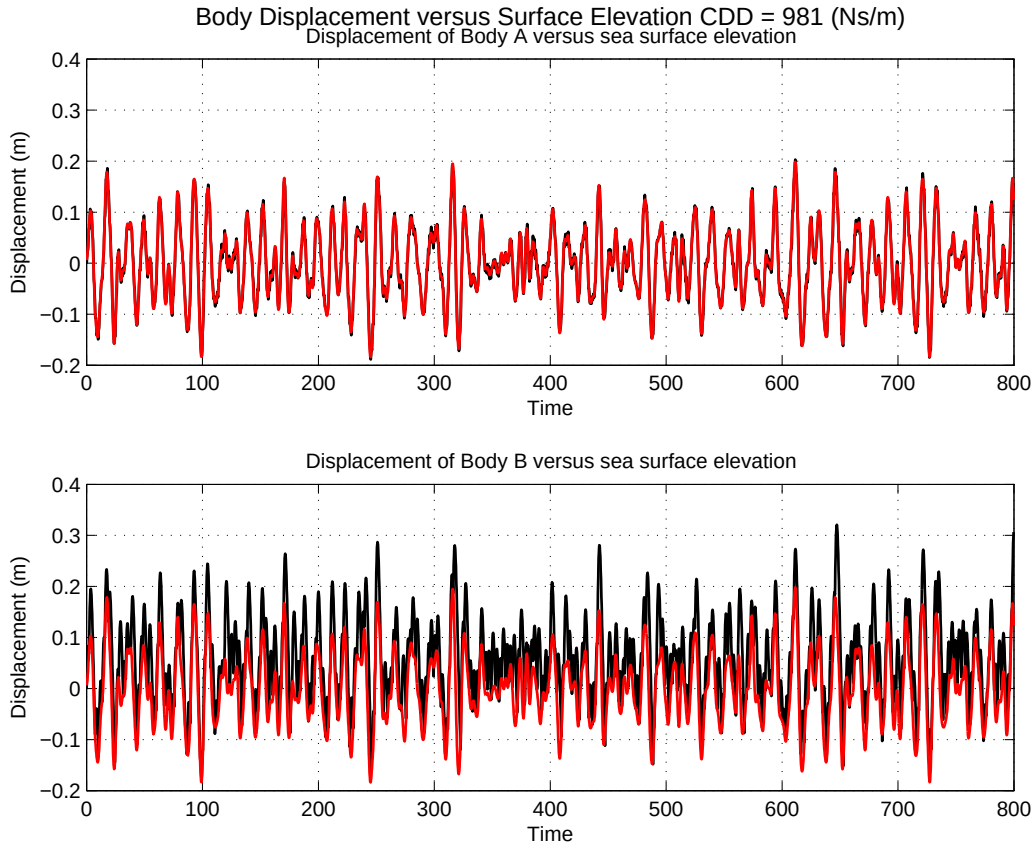

Figure 4.32. Body A and Body B heave displacement versus surface elevation

The relative displacement is shown in Fig. 4.33. The positive relative displacement is only a few centimeters and has a similar amplitude compared with the experimental data. More peaks are predicted by the numerical model than seen in the experimental data.

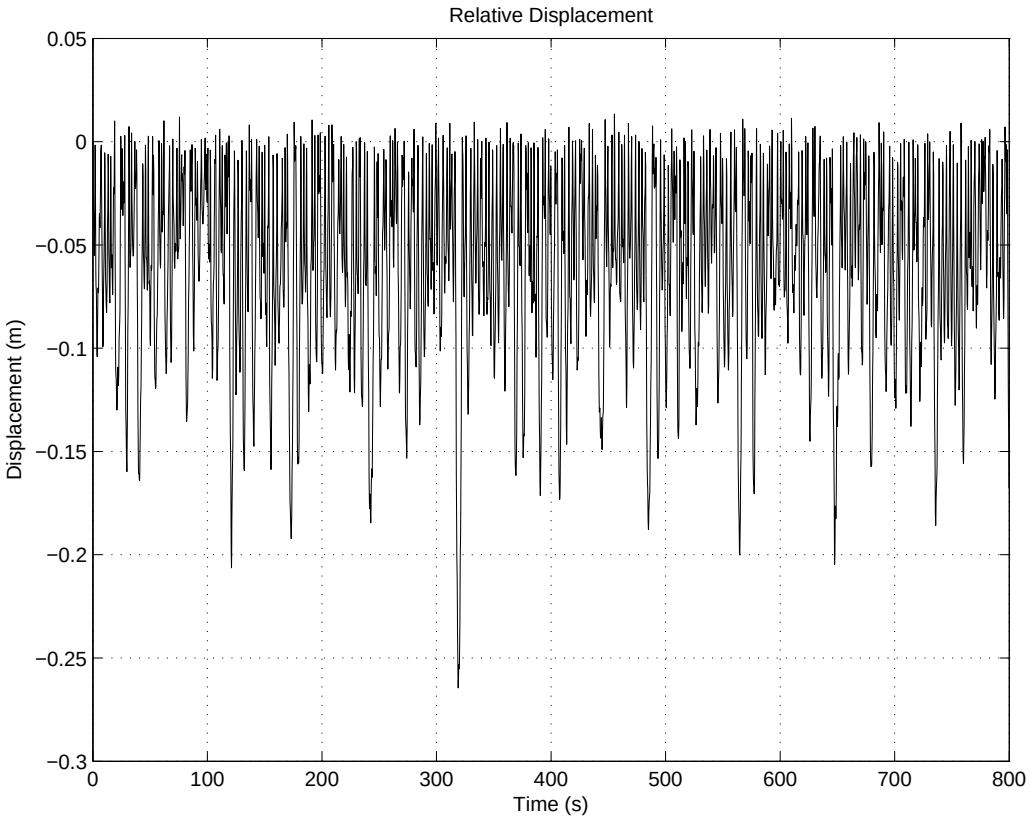

Figure 4.33. Relative displacement

The resulting time series of power output is:

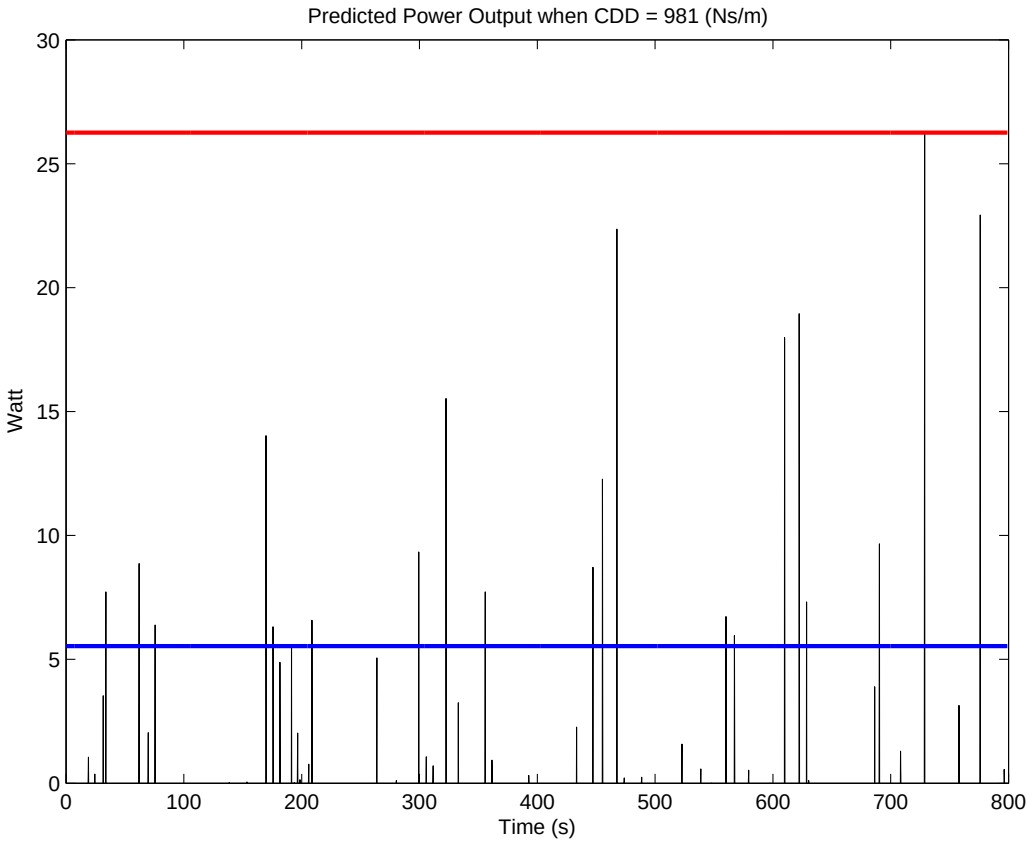

Figure 4.34. Time series of double-body power output

The maximum power output in Fig. 4.34 is around 35 W and average peak output over the time series is 6.9 W, which is slightly higher than the experimental peak power output in Fig. 4.6. The average peak output over the time series matches with the average peak output over the experimental data, but the larger peaks are not seen in the experimental data. The maximum peak power output and the average peak output are shown by the red and blue lines, respectively.

The spectrum of the relative displacement between Body A and Body B is shown with the spectrum of the surface waves in Fig. 4.35.

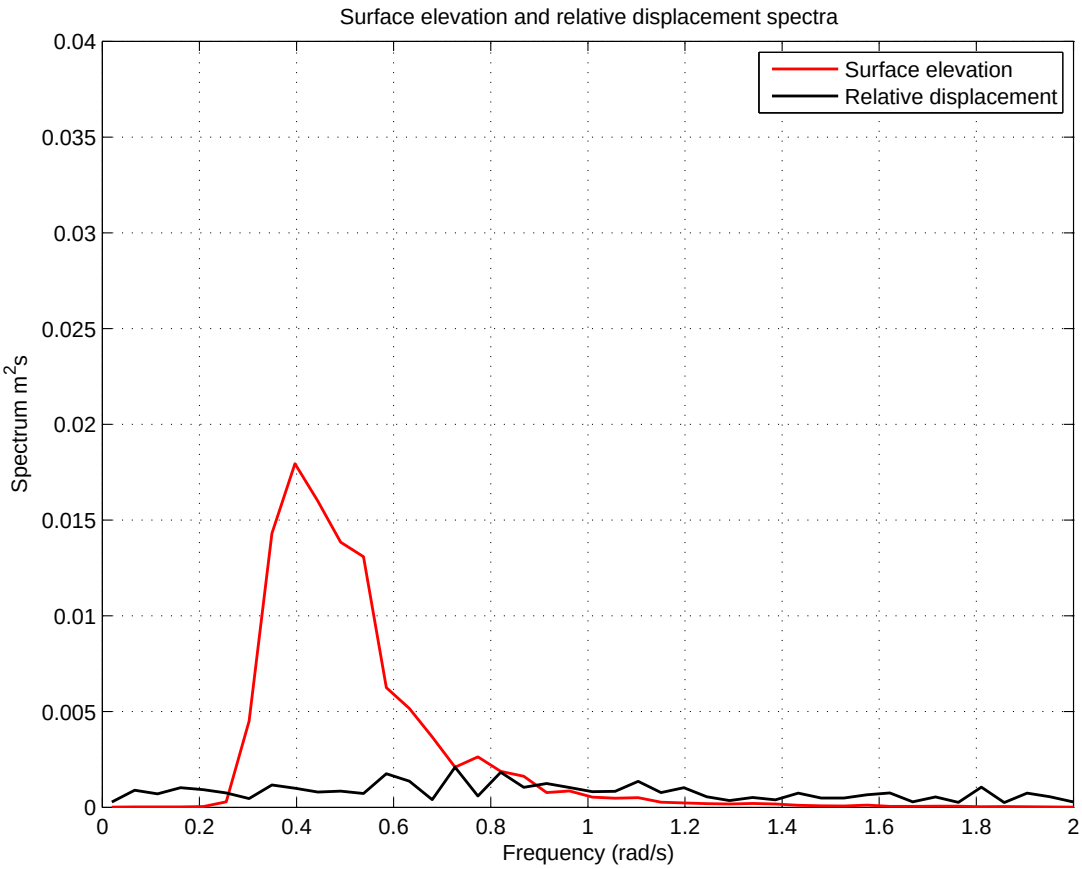

Figure 4.35. Relative displacement spectra versus surface waves

As seen in Fig. 4.35, the double-body case does not have a peak frequency, but shows a more level response. Slightly more energy is seen at the lower frequencies, when the waves are longer and there is more time for the connecting line to be pulled taut and Body A to have a greater displacement than Body B. Table 4.3 shows that the significant double amplitude, Z_s, of the relative displacement of the double-body case, is noticeably lower than the relative displacement of the single-body case. The double-body case cannot harness most of the energy in the surface waves because

Body B does not provide a consistent anchor point, unlike the sea floor in the single-body case.

Relative Displacement	Significant Values (m)
Sea Surface	0.28
Single-Body Case	0.2752
Double-Body Case	0.1978

Table 4.3. Comparison of relative displacement significant values

To check the double-body program, C_{DD} and αF were set to zero so no PTO was acting on the system. Body A reacted like a floating cylinder and had an RAO or 1.0 (the same as in the single-body case) as expected. Body B sunk, which agreed with the predicted outcome, as Body B is negatively buoyant, and according to the equations of motion with no (PTO), is no longer connected to Body A.

4.2.2.1 Different PTOs

Figure 4.36 shows that the case with lower C_{DD} experiences more instances of positive relative displacement and smaller negative relative displacement. However, $C_{DD} = 2000Ns/m$ and $1500Ns/m$ have larger positive relative displacements. Also the larger the C_{DD} is, the more nonlinear effects affect the relative displacement. A difference is seen in the smoothness of the data. The differences are caused by the C_{DD} and $\alpha F_{constant}$ restricting the body's motion and pulling Body B up when the system has positive velocity and displacement. For smaller C_{DD} values, the body's motion is very close to the sea surface elevation and the body acts like a linear system.

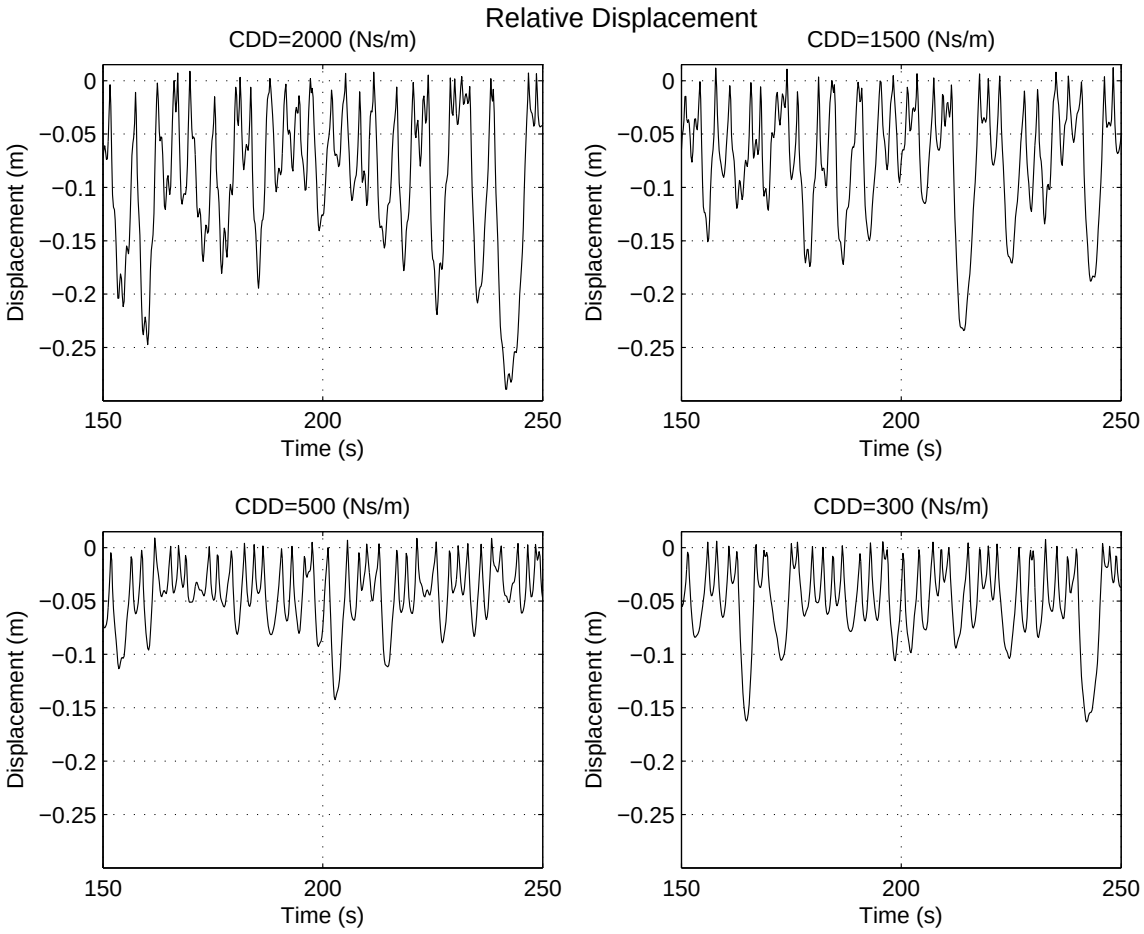

Figure 4.36. Relative displacement for various C_{DD} values

Similarly to the relative displacement, the larger the C_{DD} is, the more nonlinear effects affect the relative velocity. A difference is seen in the smoothness of the data. The differences are caused by the C_{DD} and $\alpha F_{constant}$ restricting the body's motion and pulling Body B up when the system has positive velocity and displacement.

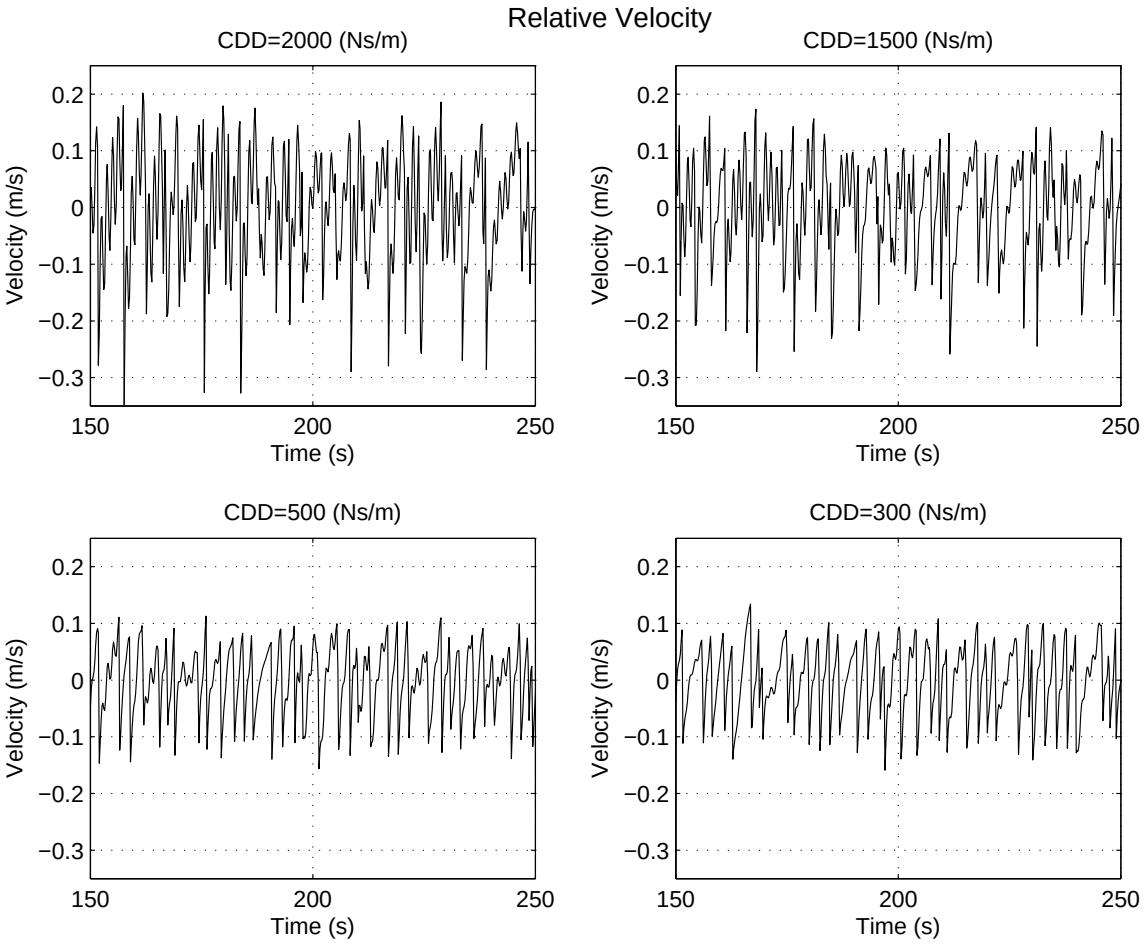

Figure 4.37. Relative velocity for various C_{DD} values

Figure 4.38 and 4.39 show the positive relative displacement and relative velocity, respectively, when power generation occurs (relative displacement and relative velocity are positive at the same time). Figures 4.38 and 4.39 show that $C_{DD} = 2500Ns/m$ is not ideal for the WEC system as there are no instances where the relative displacement and relative velocity are both positive at the same time. Therefore the system is overdamped. Similarly to the single-body case, as C_{DD} decreases, increases are

seen in the relative velocity and the number of instances of positive relative velocity. Therefore, for power generation, a tradeoff has to be made between the C_{DD} value and the velocity. Figure 4.37 shows that the smaller C_{DD} experiences more instants of positive relative velocity, and larger relative velocities. The plots of relative displacement (during power generation) show that as C_{DD} decreases, the relative displacement during power generation decreases, but the number of instances of positive relative displacement increases. This means that the lower the C_{DD} values are, the more Body B is able to act as a stable anchor point.

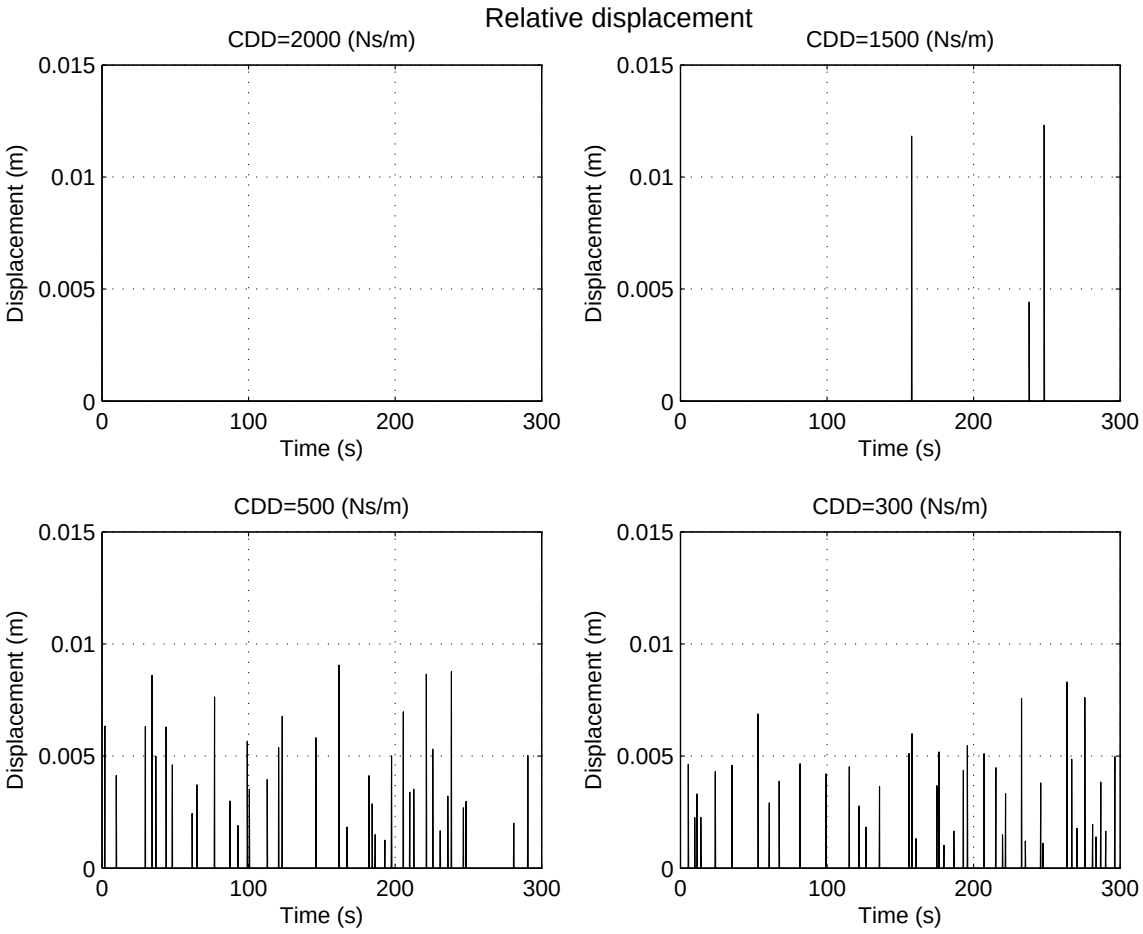

Figure 4.38. Relative displacement (during power generation) for various C_{DD} values

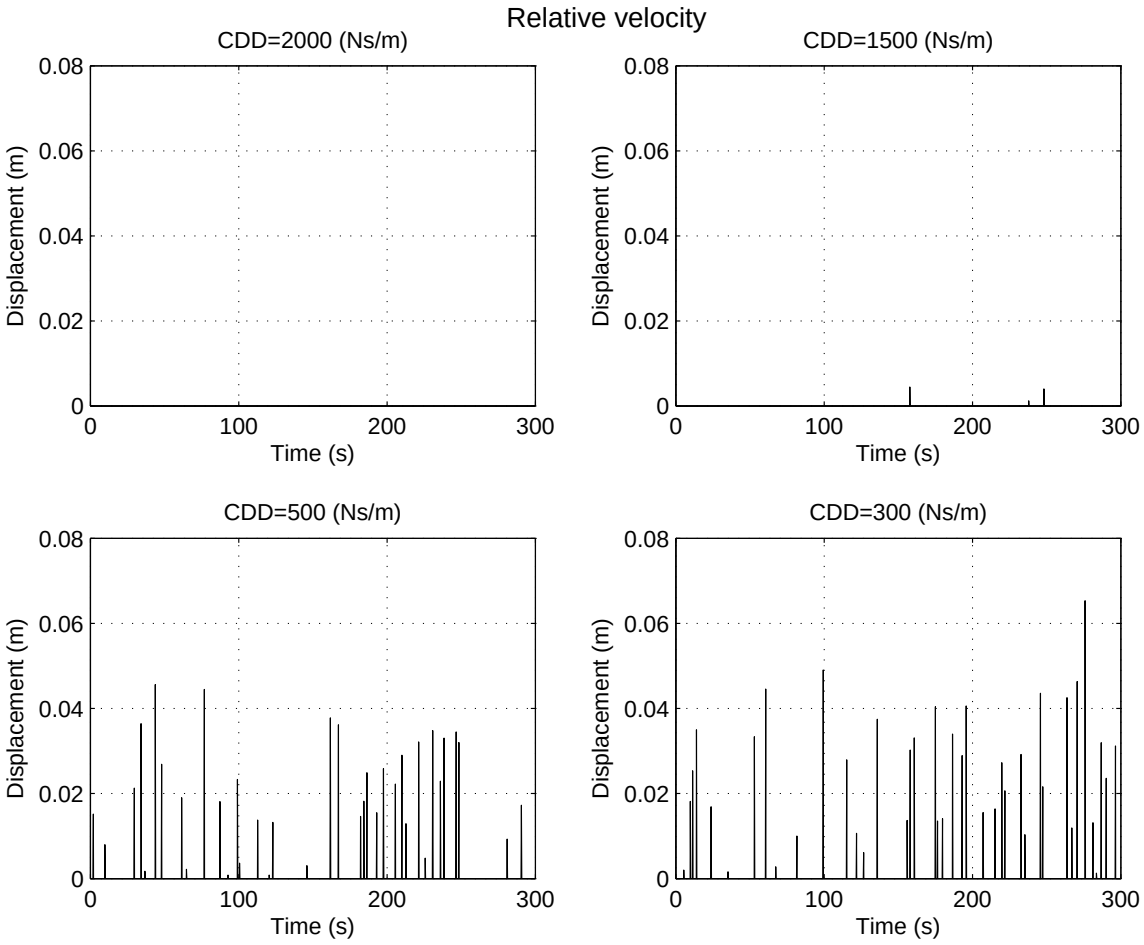

Figure 4.39. Relative velocity (during power generation) for various C_{DD} values

The overdamping with $C_{DD} = 2500Ns/m$ is easily seen in Fig. 4.40, as no power is produced because of the restricted motion. In this case, power is increasing with decreasing C_{DD}. The value of $C_{DD} = 500Ns/m$ produces the greatest magnitude peaks and the greatest amount of peaks. It seems that an optimum C_{DD} for the double-body case is $500Ns/m$.

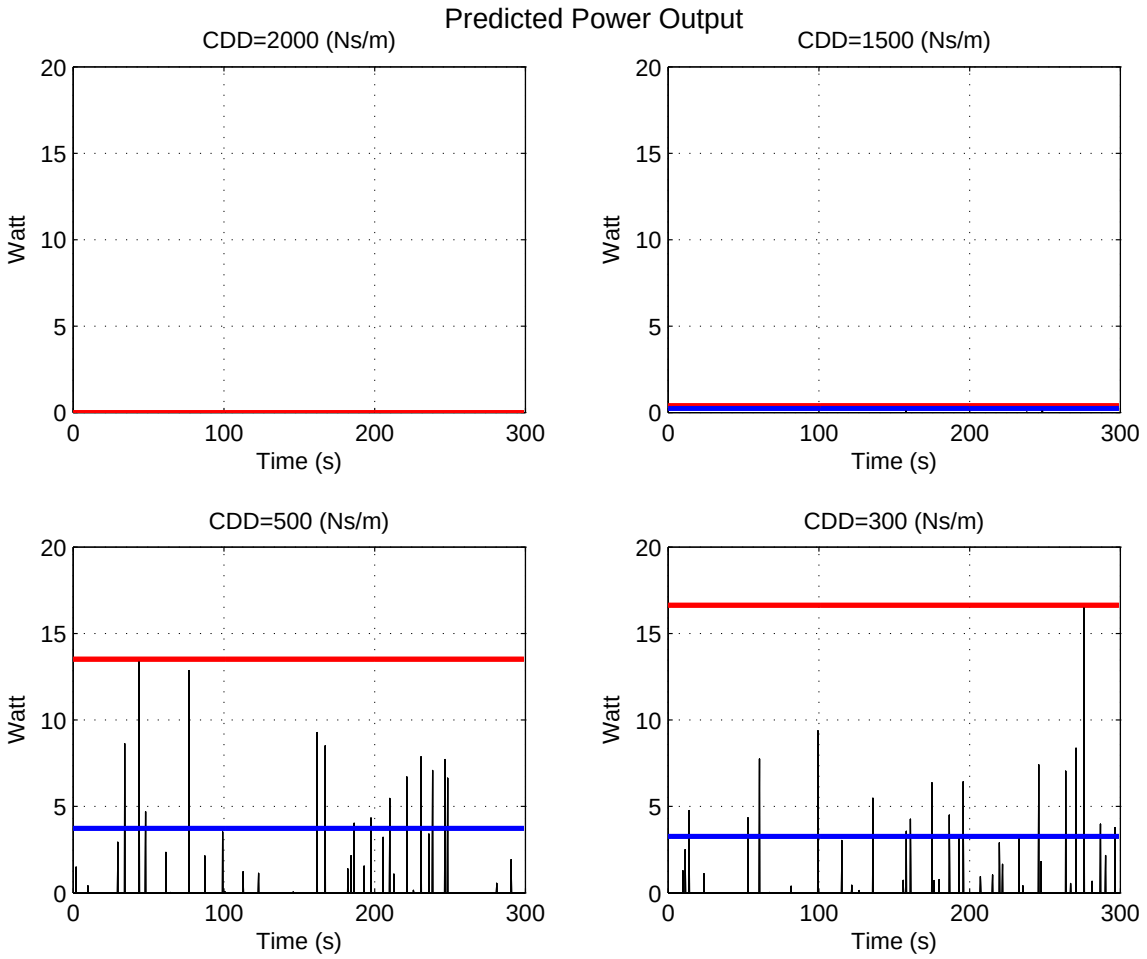

Figure 4.40. Power output for various C_{DD} values

For each case, the maximum peak power output and the average peak output are shown by the red and blue lines, respectively.

Furthermore, when the ballast weight of Body B was increased, there was a noticeable improvement in the RMS of power. However, caution should be taken not to add too much weight to the drogue. The numerical model cannot determine if a drogue would collapse from too much ballast weight.

4.2.2.2 Different Double-Body Case Conditions

A second drogue case was numerically considered to determine if it could produce more consistent and higher power. The dimensions of this drogue are governed by the conclusions of Montgomery and Stroup (1962). The downstream spill hole should be 5% of the inlet hole (for the best stability in lateral oscillations), and a height to major diameter ratio of 2 for vertical oscillation stability. The new drogue has a 2 m height, 1 m diameter large spill hole, and 0.05 m small spill hole. Montgomery and Stroup (1962), Vachon (1973), and Holler (1985) stress the importance of the H/D ratio, where H is the height of the drogue and D is the inlet (large) diameter of the drogue, on the drag coefficient and stability of the drogue. Vachon (1973) used a ratio of H/D=2, as suggested by Montgomery et al. (1962). Holler (1985) tested a range of H/D ratios and confirmed that C_D increases with the elongation of the drogue. The experimental data of Vachon (1973) and Holler (1985) agree for the corresponding H/D ratios. Holler's (1985) graph of the relation between C_D and H/D is used here to find the drag coefficient of 1.5 (H/D=1.7) for the experimental drogue, and a drag coefficient of 1.6 (H/D=2) is used for the numerical drogue.

Also, the two drogues were tested for two different depths and water depths(the experimental drogue depth and water depth and 100 m drogue depth and 5000 m water depth. For the deeper testing, it is assumed that the drogue remains directly below the WEC system. The results are shown in Table 4.4.

Cases	Experimental 10.6m	Larger Drogue 10.6m	Experimental 100m	Larger Drogue 100m
Average of Power Peaks	4.039 W	13.14W	5.26 W	5.15 W
Maximum Peak Power	14.03W	141.3 W	21.8 W	23.1 W
Power RMS	0.65 W	3.78 W	0.94 W	1.05 W

Table 4.4. Comparison between different drogues

As excepted, the larger drogue had a greater RMS. However, when deeply submerged and in deep water, there is very little difference between the two drogues.

CHAPTER 5

CONCLUSIONS AND RECOMMENDATIONS

5.1 Conclusions

5.1.1 Experimental Conclusions

The WEC system provided a maximum power output of 87 W for a 50Ω load from one power take-off device when moored in 0.3 m to 0.6 m seas. In a production model, the WEC system would have two power take-off devices which could result in a maximum power output of 174 W when moored in 0.3 m to 0.6 m seas. A smaller resistive load in the WEC system will produce even greater power. A typical Gel lead acid battery has a resistive load of 2.4Ω or smaller. The WEC system would be able to trickle charge the batteries of a buoy, which would increase the design life, and save on the maintenance costs.

A freely floating WEC system anchored to a drogue would produce less power than a moored WEC. However, with proper drogue depth and sizing, the authors' conjecture is that the freely floating WEC system could have power output similar to a moored WEC system, and be able to trickle charge batteries.

A band-pass filter smoothes the clipped sections of the WEC system's heave displacement. The filtered data creates a less noisy spectrum and a smooth RAO. The WEC system would have an RAO of 1.0 (similar to a slender circular cylinder) for periods greater than 10 s if not for the power take-off device. The power take-off

device created a damped spectrum and dip in the RAO by taking energy from the wave and converting it into electrical energy.

5.1.2 Numerical Conclusions

Comparing the single-body case with the experimental case produces similar time series motion amplitude results, as seen in Figs. 4.3, 4.7, and 4.20. The major difference is the clipping observed in the experimental data. Without this "clipping", the WEC system motion would be smoother and follow the surface elevation. Also S_z would be below S_{se}.

The numerical models are validated by the experimental data. When programmed for the wave climate of the day of the experiment, similar results for motion and power output are found for the single-body case.

For the double-body case, the relative displacement amplitude and average peak power correspond to experimental data. However, a greater amount and amplitude of the power peaks are seen in the numerical data. Using the numerical model, an optimum C_{DD}, ballast weight, and $\alpha F_{constant}$ can be found for each wave climate and used in future testing. In the double-body case, we also calculated multiple drogue designs and showed that a larger drogue is more stable and has a larger RMS at a shallower depth.

Comparing the spectra of the two cases, the single-body case is able to capture more of the available energy from the surface waves. The sea floor provides a stable

anchor point (for the single-body case) that allows for large relative displacement in the presence of the surface waves. The experimental Body B does not provide a stable relative anchor point for Body A. It appears that a limiting factor in the double-body case is the ability of Body B to have limited response to the PTO force and wave exciting forces.

5.2 Recommendations

In future works, the double-body case should be tested with a larger drogue and deeper water. The next testing phase should extend the experiments for a longer period of time, and possibly incorporate a rechargeable battery to store the intermittent power. Also, both cases should be tested in multiple sea states. Furthermore, multiple drogue shapes should be tested to determine which shape will provide the best anchor point.

REFERENCES

Celesco (2012), Rotational position transducer RT8101. May 2012. url:http://www.celesco.com/datasheets/rt8101.pdf.

Chitrapu, S. A. (1992), *Nonlinear Forces and Response of Floating Platforms in Regular and Random Waves*, Ph.D. thesis, University of Hawai'i at Manoa, Department of Ocean Engineering, Honolulu, HI.

Chitrapu, S. A. and Ertekin, R. C. (1995), Time-Domain Simulation of Large-Amplitude Response of Floating Platforms, *Ocean Engineering*, Vol. 22, pp. 367–386.

Davis, E., Ertekin, R. C., and Riggs, H. R. (2009), A Buoy-Based WEC Device to Provide Low Power to Sensors, In *Proc, 28th International Conference on Ocean, Offshore and Arctic Engineering*, OMAE, ASME.

Eagletree Systems (2012), eLogger V4 and PowerPanel. May 2012. url:http://www.eagletreesystems.com/micropower/details.htm.

Engelmann, M. (2012), Trex Enterprises:Personal Communication .

Engelmann, M., Davis, E., and Symonds, D. (2011), Non-Resonant, Rotary-Drive Wave Energy Conversion Device for Distributed Remote Sensing and Communications Applications, In *Proc. of Oceans'11*, pp. 1–4, MTS-IEEE.

Greeson, D. (1997), *The Relative Motion of Two Adjacent Bodies, One Significantly Larger Than The Other, Floating in Waves, with a Non-Linear Line Connection*, Ph.D. thesis, University of Hawai'i at Manoa, Department of Ocean and Resources Engineering, Honolulu, HI.

Holler, R. A. (1985), Hydrodynamic Drag of Drogues and Sea Anchors for Drift Control of Free-Floating Buoys, In *Proc. of Oceans'85 - Ocean Engineering and the Environment*, pp. 1330–1335, IEEE.

HYDRAN (2008), A Computer Program for the HYDroelastic Response ANalysis of Ocean Structures, v. 3.9.3r2, OffCoast, Inc., Kailua, Hawaii.

Keller, V., Numerical Model of a Wave Energy Conversion Device, Master's Plan B Paper, Department of Ocean and Resources Engineering, University of Hawaii at Manoa, August 2011.

Madgetech (2012), Volt101A-160mV data logger. May 2012. url:http://www.madgetech.com/pdffiles/datasheets/volt101adifds.pdf.

McCormick, M. (1981), *Ocean Wave Energy Conversion*, New York, Wiley-Interscience.

Ming Tai Industrial Co (2012), Constant Force Spring, Sept 2012, URL:www.powerspring.com.tw.

Montgomery, R. B. and Stroup, E. (1962), *Equatorial Waters and Currents at 150 W in July-August 1952*, Baltimore, Johns Hopkins Press.

NASA (2013), Ocean Motion and Surface Currents. Drifers and Buoys Dec 2012. url:oceanmotion.org/html/gatheringdata/buoysanddrifers.htm.

NOAA (2012), National Weather Service, June 2012, url:www.noaa.gov/.

Nolte, J. D., Ertekin, R. C., and Davis, E. (2013), In-Ocean Experiments of a Wave Energy Conversion Device when Moored to an Anchor and to a Drogue, *Journal of Ocean Technology*, Vol. 8, No. 1, pp. 71–85.

Nortek AS (2012), Data sheet: Aquacopp current meter. May 2012. url: http://www.nortek-as.com/lib/data-sheets/datasheet-aquadopp.

Ogilvie, T. F. (1964), Recent Pogress Toward the understanding and Prediction of Ship Motions, In *Proc. 5th Symp. of Naval Hydrodynamics*, pp. 3–128.

Otto de Kat, J. (1988), *Large Amplitude Ship Motions and Capsizing in Severe Sea Conditions*, Ph.D. thesis, University of California, Naval Architecture and Offshore Engineering, Berkeley, CA.

Pawlak, G. (2012), Personal Communication, University of Hawai'i at Manoa, May 2012.

Salter, S. H. (1978), The Development of the Duck Concept, In *Wave Energy Conference*, pp. 17–44.

Symonds, D., Davis, E., and Ertekin, R. C. (2010), Low-Power Autonomous Wave Energy Capture Device for Remote Sensing and Communications Applications, In *Proc of IEEE Energy Conversion Congress and Exposition*, pp. 2392–2396,

IEEE.

Vachon, W. A. (1975), Instrumented Full-Scale Tests of a Drifting Buoy and Drogue, Technical report, The Charles Stark Draper Laboratory, Inc., Massachusetts.

Vachon, W. A. (1977), Current Measurement by Lagrangian Drifting Buoys-Problems and Potential, In *Proc. of Oceans'77*, pp. 46B1–46B7, MTS-IEEE.

Van Oortmerssen, G. (1979), Hydrodynamic Interaction Between Two Structures, Floating in Waves, In *Proc. Second International Conference on Behaviour of Off-shore Structures*, pp. 347–356.

Vicente, P. C., Falcao, A., and Justino, P. (2010), Nonlinear Dynamics of a Tightly Moored Point-Absorber Wave Energy Converter, In *Proc, ASME 2010 29th International Conference on Ocean, Offshore and Arctic Engineering*, OMAE, ASME.

Washio, Y. (1998), Wave Energy Research and Development at JAMSTEC. Sept 2012. URL:http://www.takesteps.org.